AGU PUBLICATIONS

Journal of Geophysical Research: Planets

Supporting Information for

Sub-diurnal methane variations on Mars driven by barometric pumping and planetary boundary layer evolution

J. P. Ortiz[1,2], H. Rajaram[2], P. H. Stauffer[1], K. W. Lewis[3], R. C. Wiens[4], D. R. Harp[5]

[1]Energy and Natural Resources Security, Los Alamos National Laboratory, Los Alamos, NM, USA
[2]Dept. of Environmental Health and Engineering, The Johns Hopkins University, Baltimore, MD, USA
[3]Dept. of Earth and Planetary Sciences, The Johns Hopkins University, Baltimore, MD, USA
[4]Earth, Atmospheric, and Planetary Sciences, Purdue University, West Lafayette, IN, USA
[5]The Freshwater Trust, Portland, OR 97205, USA

Contents of this file

1. Generating Synthetic Pressures and Temperatures

To treat the problem more generally, we generated synthetic pressures and temperatures to use as boundary conditions in the simulations. Our first step in processing was to perform an elevation-pressure correction due to change in *Curiosity* rover's position in time. We gathered rover positional data, then calculated the relative pressure offset caused by elevation change using a simple air-static condition: $p(z) = p_0 + \rho_{air} g z$, where $p(z)$ is the adjusted air pressure [Pa], p_0 is the air pressure [Pa] at the landing site, ρ_{air} is approximate air density [kg m^{-3}] at the landing site, g is acceleration due to gravity [m s^{-2}], and z is the elevation [m] relative to the landing site. This procedure is described in detail in Ortiz et al. (2022).

We then performed an initial decomposition of the pressure and temperature data into the frequency domain using a Fast Fourier Transform (FFT) algorithm (Cooley & Tukey, 1965) to get a preliminary estimate of the dominant harmonic components. Plots showing the results of spectral decomposition are shown in Figure S1 and Figure S2.

To generate synthetic pressure and temperature records, we compose a summation of sinusoidal components described by their frequency (ω), amplitude ($\mathcal{A}$), and phase (γ). We determined the exact components to use by optimizing the root mean squared error of the synthetic data to the observed (elevation-adjusted) pressures and temperatures. We started with the dominant periods determined from the FFT decomposition above, and then and calibrated ω, $\mathcal{A}$, and γ by minimizing the root mean squared error (RMSE) using the differential evolution algorithm (Storn & Price, 1997). An initial calibration used a single diurnal amplitude for the barometric pressures (i.e., pressure amplitude of the diurnal component did not vary seasonally), which caused significant mismatch because the diurnal amplitudes are not constant throughout the Mars year. We therefore used a seasonally modulated synthetic barometric pressure signal, following Harp, Ortiz, and Stauffer (2019):

$$P_s(\theta) = \left(\mathcal{A}_d + \mathcal{A}_s \sin\left(\omega_s t + \gamma_s\right)\right) \sin\left(\omega_d t + \gamma_d\right), \tag{1}$$

where P_s is the synthetic signal, $\mathcal{A}_d$ is the mean diurnal amplitude of given frequency, $\mathcal{A}_s$ is the amplitude of the seasonal modulation, ω_d is the diurnal frequency, ω_s is the seasonal modulation frequency (seasonal period, $T_s = 1$ Mars year, where $\omega_s = 2\pi/T_s$), γ_d and γ_s are the phase shift of the dominant frequency and seasonal modulation, respectively, and $\theta = [\mathcal{A}_d, T_d, \gamma_d, \mathcal{A}_s, \gamma_s]$ is a vector containing the calibration parameters, for which we aim to minimize an objective function $F(\theta)$ comparing the measured pressures/temperatures to the synthetic values. It is the $(\mathcal{A}_d + \mathcal{A}_s \sin(\omega_s t + \gamma_s))$ term that captures the seasonal modulation about the mean dominant frequency. The objective function F minimized in the calibration is the root mean squared error.

2. Heat Flow Verification

In this section, we describe several heat flow verification tests that we performed. The purpose of these tests is two-fold: to ensure that the physics are represented correctly in the FEHM simulator, and to generate confidence in the formulation of our model, which sequentially coupled the heat model to the flow and transport model.

2.1. Conductive Heat Flow Verification

The first step in implementing temperature-dependent adsorption in FEHM is to verify that the heat flow model behaves as expected. We perform a heat flow verification test using a simple problem in a 1-meter square domain (Figure S5) with initial, uniform temperature $T_0 = 200°$C. From time $t > 0$, the top and right boundaries of the box are assigned a constant $T = 100°$C, with zero heat flux boundary conditions on the left and bottom boundaries. We then observe the temperature decay two observation points (Figure S5).

The analytical solution for the temperatures in this 2-D heat conduction problem is given by Carslaw and Jaeger (1959):

$$T = T_s + \frac{16(T_0 - T_s)}{\pi^2} \sum_{m=0}^{\infty} \sum_{n=0}^{\infty} \frac{(-1)^{m+n}}{(2m+1)(2n+1)} \cos\frac{(2m+1)\pi x}{2a} \cos\frac{(2n+1)\pi y}{2b} e^{-\alpha_{m,n} t} \tag{2}$$

where $\alpha_{m,n} = \frac{\kappa\pi^2}{4}\left[\frac{(2m+1)^2}{a^2} + \frac{(2n+1)^2}{b^2}\right]$ and the region is taken to be $-a < x < a$, $-b < y < b$.

2.2. Verification of Subsurface Temperatures

We then verify that we are able to reproduce the expected subsurface temperature variations driven by surface temperature changes predicted by an analytical solution. As thermal waves propagate through the subsurface, their amplitude diminishes exponentially with depth from the surface. In the analytical solution discussed in Jones, Lineweaver, and Clarke (2011), the surface heat variations can be modeled as sinusoidal curves:

$$T_s(t) = T_0 + \Delta T \cos(\omega t) \tag{3}$$

where T_s is the surface temperature, T_0 is the mean surface temperature, ΔT is the amplitude of temperature variation about the mean, and ω is the angular frequency ($\omega = 2\pi f$, where f is the frequency (i.e., cycles per sol, cycles per year) of the temperature signal. The subsurface temperatures are then given by:

$$T_{sub}(y,t) = T_0 + \Delta T \exp\left(-\frac{y}{d_\omega}\right) \cos\left(\omega t - \frac{y}{d_\omega}\right) \tag{4}$$

where y is depth beneath the surface [m], d_ω is the thermal skin depth ($d_\omega = \sqrt{\frac{2\alpha}{\omega}}$) where the thermal diffusivity $\alpha = \frac{\kappa}{\rho c_p}$, where κ is thermal conductivity, ρ is density, and c_p is specific heat capacity.

We simulated surface thermal wave propagation in to the subsurface using a homogeneous domain with the following properties: $\kappa = 2.5$ W/(m $\cdot$ K), $\rho = 2900$ kg m^{-3}, $c_p = 800$ J/(kg $\cdot$ K). For the surface forcing, we used a period of 1 day (period = $\frac{\omega}{2\pi}$), and $\Delta T = 10$ °C. Our results in Figure S7 show good agreement between simulated and analytical subsurface temperatures. We performed verification at several longer periods (up to annual) for temperature forcing that are not shown here, but likewise indicated good agreement with the analytical solution.

2.3. Pure Conduction vs Conduction-Convection

The adsorption mechanism is dependent on temperature, which is dependent on depth below ground surface and time. Using the surface temperatures collected by *Curiosity*, we simulate transient 2D heat flow in the subsurface by comparing simple conduction to matrix conduction/fracture convection in a single-fracture model. Because of the high level of mesh refinement required for accurate representation of heat flow, we wanted to be able to simulate the subsurface temperatures (with a fine mesh) using a 1-D model, implicitly ignoring the effects of fractures. To determine if this can be done with without sacrificing accuracy, we needed to show that convective heat transfer effects is negligible compared to the overall effects of conduction.

We compared the subsurface temperature perturbation depths for these cases to determine whether subsurface convection can be considered negligible. In the case that convection is negligible, we can likely perform separate simulations for heat flow and methane transport (sequential coupling) rather than perform a fully-coupled thermo-physico-chemical simulation, which would be more computationally demanding. It is likely that a pure conduction model will sufficiently capture the subsurface temperature behavior; previous work has estimated that the seasonal thermal skin depth does not extend down to more than a few meters (Mellon & Phillips, 2001; Meslin et al., 2011; Moores et al., 2019; Gough et al., 2010). Nevertheless, it was important for us to perform this check since the presence of fractures may cause the thermal skin depth to be deeper than previous estimates, at least along the fractures.

The pure, single-phase heat conduction equation is as follows:

$$\frac{\partial T}{\partial t} = \alpha \nabla^2 T \tag{5}$$

where T is the temperature [K], t is time [s], and α is the thermal diffusivity coefficient [m^2 s^{-1}] ($\alpha = \frac{\kappa}{c\rho}$, where κ is the thermal conductivity of the material [J s^{-1} m^{-1} K^{-1}], c is the specific heat capacity [J K^{-1} kg^{-1}], and ρ is the density of the material [kg m^{-3}]).

In the case where flowing air currents in porous media transport significant amounts of heat, the energy conservation equation for conduction-diffusion is as follows:

$$[(1-\phi)\rho_r c_{pr} + \phi \rho_v c_{pv}] \frac{\partial T}{\partial t} = \nabla \cdot (\kappa \nabla T) - \nabla \cdot (\vec{v} \rho_v h_v) \tag{6}$$

where ϕ is matrix porosity [–], ρ_i is the density for rock (r) or vapor (v) [kg m^{-3}], respectively, c_{pi} is the specific heat capacity for constituent i [J K^{-1} kg^{-1}], T is temperature [K], t is time [s], κ is thermal

conductivity of the rock [J s^{-1} m^{-1} K^{-1}], h_v is the specific enthalpy of the vapor [m^2 s^{-2}], and ∇ is the gradient operator. The fluid velocity vector $\vec{v}$ is assumed to follow Darcy's law:

$$\vec{v} = -\frac{k}{\mu_v}\left(\nabla P - \rho_v \vec{g}\right), \tag{7}$$

where k is the rock permeability [m^2], μ_v is the dynamic vapor viscosity [Pa s], P is pressure [Pa], and $\vec{g}$ is the gravitational acceleration vector [m s^{-2}]. In (6), we assume instantaneous thermal equilibration between the rock and the fluid.

2.3.1. Thermal Péclet Number Analysis

The above result makes intuitive sense if we consider the thermal Péclet number, a dimensionless number that quantifies the relative importance of conduction and convection:

$$\mathrm{Pe}_T = \frac{uL}{\alpha} \tag{8}$$

where u is the fluid flow velocity [m s^{-1}], L is the characteristic length [m], and α is the thermal diffusivity [m^2 s^{-1}] ($\alpha = \frac{\kappa}{\rho c_p}$, where κ is the thermal conductivity, ρ is the bulk density, and c_p is the specific heat capacity).

We calculate an approximate velocity of air flow (u) in the subsurface using the single-fracture, double-porosity pressure response solution in (Equation 8 in Nilson et al., 1991). The air flow velocity is the key quantity in heat convection for this problem, and we assume that the air flow is driven by the barometric pressure gradient at ground surface. We use representative values for a diurnal pressure perturbation (period = 1 sol, ΔP = 40 Pa, mean pressure P_0 = 800 Pa). For the subsurface we use properties representative of our flow and transport simulations: fracture aperture δ_f = 1 mm, fracture spacing δ_m = 5 m, matrix permeability $k_m = 10^{-14}$ m^2, and matrix porosity ϕ_m = 0.35. To estimate the air flow velocity using equation 8 from Nilson et al. (1991), we calculate the pressure gradient at 30 m and 5 m depth, with 2 mm lateral displacement from the fracture. We set the characteristic length L to the respective depth at which we calculated the flow velocity.

Rock Thermal Properties:

Rock thermal properties were taken as: density ρ_r = 2900 kg m^{-3}, thermal conductivity κ_r = 2.7 W / (m · K), and specific heat capacity c_p = 800 J / (kg · K). The rock thermal diffusivity α_r, then, is 1.16×10^{-6} m^2 s^{-1}.

Air Thermal Properties:

Mars air thermal properties were taken as: density ρ_a = 0.018 kg m^{-3}, thermal conductivity κ_a = 0.01663 W / (m · K), and specific heat capacity c_p = 849 J / (kg · K). The air thermal diffusivity α_a, then, is 1.03×10^{-3} m^2 s^{-1}.

Bulk Thermal Properties:

To estimate the thermal response of the subsurface as a whole, we calculate thermal properties of the subsurface in bulk, taking into account both the fluid (air) volume (V_a) and the solid volume (V_r). The bulk density ρ_b = 1884 kg m^{-3}, bulk thermal conductivity ($\kappa_b = (\kappa_a V_a + \kappa_r V_r)/V_{total}$) is 1.76 W / (m · K), and bulk specific heat capacity c_p = 817 J / (kg · K). The bulk thermal diffusivity α_b, then, is 1.14×10^{-6} m^2 s^{-1}.

At 30 m depth, the maximum velocity, u, in the matrix is 1.1×10^{-9} m s^{-1}. Using this depth for L, we calculate a thermal Péclet number of ~ 0.027, which indicates that conduction should dominate over convection. At 5 m depth, the maximum velocity $u = 3.1 \times 10^{-9}$ m s^{-1}. Using this depth for L, we calculate a thermal Péclet number of ~ 0.011, which similarly indicates that conduction should dominate over convection. This result is not surprising; one would expect that the heat capacity in the system is dominated by the matrix/rock solids rather than the low-density CO_2 carrier gas. Although air flow velocities in the fractures are orders of magnitude greater than the velocity in the rock matrix, the fractures make up a relatively small portion of the total porosity and, thus, a small portion of the energy transport. If the flowing fluid were a liquid, rather than a gas, a much greater portion of heat transport would be due to convection, and likely could not be considered negligible.

2.4. Effect of Temperature on Air Flow Properties

Due to increased computational costs associated with performing fully-coupled thermo-physico-chemical simulations, we chose to perform sequentially-coupled simulations by running heat flow first, then applying the calculated subsurface temperatures as boundary conditions for the adsorption mechanism in the flow and transport model. The temperatures are applied to the isothermal flow and transport simulations by varying the Langmuir adsorption coefficients in the adsorption process based on the ambient temperature. In reality, temperature would also affect fluid properties such as density and viscosity, which could affect flow and transport. From the CO_2 equation of state, we calculated that a 50 °C change in temperature results in only a 0.96% change in density from reference conditions $T = -50$°C and $P = 700$ Pa. The same temperature change results in a 22% change in viscosity. Although this seems like a large effect, the actual amplitude of the temperature changes in the subsurface is much smaller.

3. Modified Dual-Enrichment Run Procedure

The typical dual-enrichment run is described in Webster et al. (2018a). It involves first the evacuation of the Herriott cell, followed by opening of an inlet to the ambient atmosphere. The ingested atmospheric sample is passed through scrubbers to remove CO_2 and H_2O before entering the Herriott cell, eventually reaching 5–6 mbar after 2 hours. This results in an enrichment in the CH_4 by a factor of 25. The valve to the Herriott cell is then closed and 26 spectra are taken of the sample over ∼75 min. The Herriott cell is then evacuated and another 26 spectra are taken to record "empty cell" spectra to allow subtraction of any methane contribution from the foreoptics chamber. Finally, the Herriott cell is again filled up by opening another inlet to make a direct ingest of the atmosphere without passing the sample through scrubbers. A final 26 spectra are taken of the sample before the instrument is powered down (Figure S1 in Webster et al., 2018b). The entire process takes ∼8.5 hours (shorter in daytime from less heating required).

Prior to each run, the scrubbers are cleaned up by heating. This cleanup process typically takes 2 hours 21 min.

A slightly modified procedure would introduce two changes to the typical dual-enrichment run:

1. The direct ingest segment would be dropped. The direct ingest measurements were a low-resource way to observe CH_4 spikes in coordination with TGO measurements, but this is not expected to be very useful in answering the question at hand. Leaving out the direct ingest segment would conserve pump life and reduce the runtime of the experiment by ∼100 min to ∼7 hours.

2. Spectra would be taken over the two hours as the Herriott cell is being filled for the enriched measurements ("ingest scans"). These scans would be taken at the same cadence as the sets of 26 scans. These ingest scans serve two purposes. Firstly, they can also provide another way of quantifying the background CH_4 levels. Secondly, the scans could be used to detect any drastic changes in the ambient VMR that may occur.

The long duration of the enrichment run and the scrubber cleanup, in addition to the large power requirements, make it difficult to conduct more than one run within a single sol. The next best thing would be to conduct both of our proposed dual-enrichment runs as close together as possible in order to reduce the likelihood of significant changes in local weather conditions or other factors that could impact the assumed diurnal cycle of methane at Gale.

4. Diffusive Atmospheric Mixing Model

We attempt to visually illustrate the implementation of the atmospheric diffusion model within an expanding/contracting domain (Figure S10).

We initially took a more simplified approach to the atmospheric mixing model by assuming that methane released into the column mixed instantaneously across its entire height, as was done in Moores et al. (2019). The atmospheric methane concentration is then controlled predominantly by the PBL height varying in time, as this controls the mixing volume. An issue with this approach is that the mixing time is so fast that individual methane flux pulses are not observable in terms of the resulting abundance that would be measured by SAM-TLS. While instantaneous mixing may be a reasonable approximation for when PBL conditions are extremely unstable (Lin & McElroy, 2010), a partial mixing diffusive model is likely more representative of mixing under general atmospheric conditions in response to highly transient surface flux pulses.

5. Dust Devil-Induced Flux Simulations

A gradual increase in dust devil activity has been predicted by previous research (Richardson et al., 2007) as *Curiosity* climbs the slopes of *Aeolis Mons* for the remainder of its campaign. rooted in the mechanisms behind dust devil formation. Dust devils are convective vortices that occur during periods of strong convective heating of the ground surface, specifically when the ground temperature exceeds the ambient air temperature. Heating of the ground surface warms the air directly above it, causing the air to rise. As the air rises, any existing vorticity becomes more vertical and more intense, developing a low-pressure zone at the vortex core surrounded by strong tangential winds. The winds can be assisted by the suction effect imbued by the pressure drop. Lower thermal inertias, a property representing the ability of a material to conduct and store heat, of the ground surface can be a contributing factor to increased dust devil activity, since such conditions favor larger differences between the ground and air temperatures. However, Newman et al. (2019) found that this effect was less important overall than the increase in topographic elevation, which encourages vortex formation because of the cooler near-surface daytime air temperatures.

To investigate the effects of dust devils on surface methane flux, we simulated methane transport induced by pressure drops with a range of properties representative of the REMS pressure drop data analyzed by Ordóñez-Etxeberria, Hueso, and Sánchez-Lavega (2020). From Ordonez-Etxeberria, Hueso, and Sánchez-Lavega (2018), pressure drops in the REMS record are defined by two parameters: intensity of the pressure drop, and its duration. Individual pressure drop events are extracted by numerically describing the data in terms of these parameters by fitting the pressure data with a Gaussian function in a moving window of 60 s:

$$P(t) = P_0 - \Delta P \cdot \exp\left[-\left(\frac{t - t_0}{\sigma}\right)^2\right] \tag{9}$$

where $P(t)$ is the pressure as a function of time [Pa], P_0 is the baseline/ambient pressure [Pa], ΔP is the intensity of the pressure drop [Pa] computed as the difference between P_0 and the minimum pressure value, t_0 is the time corresponding to the pressure minimum [s], and σ is related to the duration, or Full Width at Half Maximum (FWHM) of the Gaussian through $FWHM = 2\sqrt{\ln 2}\sigma$.

5.1. Boundary and Initial Conditions: Dust Devil Simulations

Because pressure drops measured by REMS typically last on the order of seconds, they require highly refined temporal resolution to simulate properly, which is numerically intensive. Therefore, rather than run multi-year scenarios with sub-second temporal resolution, we estimate the upper bounds of fluxes that could be generated by performing truncated simulations (120 s) with high temporal resolution using conditions ideal for inducing subsurface gas flux (i.e., the best case scenario for generating flux). We performed the dust devil simulations after our running our preliminary subsurface-atmosphere model simulations so that we would only have to consider fracture-rock architectures that best matched the observed atmospheric methane abundances. We populate the subsurface initially with a uniform methane concentration equal to the maximum near-surface concentration achieved in the corresponding subsurface-atmospheric transport model at steady-state. So doing essentially represents the time of year with the highest methane concentrations in the shallow subsurface, and thus the chance for the greatest fluxes vented to the atmosphere for a given drop in pressure. We prescribe an initial atmospheric pressure equal to the mean surface pressure at Gale crater. We then perform a suite of simulations with dust devil duration (FWHM) ranging from 5 to 25 s, and pressure drops ranging from 1 to 5 Pa. The timing of the pressure drop minimum (t_0) occurs halfway through the 120 s simulation.

5.2. Dust Devil Pressure Drop Results

6. Fracture Network

6.1. Fracture Generation Algorithm

We randomly generated orthogonal discrete fractures using the 2-D Lévy-Lee algorithm (Clemo & Smith, 1997), a fractal-based fracture model (Geier et al., 1988). In this model, fracture centers are created sequentially by a "Lévy flight" process, – a termed coined by Benoît Mandelbrot and named for Paul Lévy – in which the step lengths in a random walk follow the heavy-tailed Lévy distribution

(Viswanathan et al., 1999). In a similar manner, fracture center locations in the Lévy-Lee algorithm are produced by random walk, and the distance between fracture centers L' is sampled from the power law distribution:

$$P_L\left(L' > L\right) = L^{-D} \tag{10}$$

where D is a specified fractal dimension. The direction of the separation between fracture centers is uniformly distributed between 0° and 360°. Fracture length and the variation in orientation are proportional to the distance from the previous fracture. The Lévy-Lee model generates a fracture network with a continuum of scales for both fracture length and spacing between fractures and uses the same exponent for fracture trace length and spacing. Structurally, the fracture networks generated by the Lévy-Lee algorithm tend to have clusters of fractures, with tighter clusters resulting from larger values of D. Since individual fracture lengths are assigned stochastically, we generated fracture networks with the desired fracture densities using a differential evolution optimization approach (Storn & Price, 1997) to determine the number of fractures required in each domain.

This mesh was then mapped onto a 3-D grid and extended across the width of the domain in the y direction – a single cell across – since FEHM does not solve true 2-D problems. This mapping essentially embeds the fractures in the rock matrix via upscaling of properties, allowing transfer of fluids and tracers to occur at the fracture-matrix interface. This mesh was then mapped onto a uniform grid.

6.2. Fracture Network Topology

The fracture network used in this study was designed to be representative of a fractured subsurface on Mars. Without rock cores or detailed logs, we know very little about fracture networks on Mars below the surface, though it is believed to be highly fractured (Figure S12). We want to generate a fracture network such that it would have a fracture density (i.e., the ratio of fracture volume to bulk rock volume) comparable to that in Mars' subsurface. Because the subsurface on Mars is so poorly characterized, we have made estimates of the fracture density based on rover photographs depicting surface expressions of fracture networks at Gale crater using a fracture trace method (Figure S13). Because the observed surface is roughly two-dimensional – and also due to the 2-D nature of our model – we calculate an "areal fracture density" (the ratio of fracture area to bulk rock area) and assume a similar fracture distribution in cross-section. We track the area of the fracture traces relative to the total image area using a script in Adobe Illustrator (Adobe Inc., 2019). The calculated areal fracture density of the fracture network in Figure S13 was $\sim 0.1\%$. In reality, the subsurface on average will be less fractured than this view of the surface, so we consider fracture densities in our simulations in the range 0.0% to 0.035%.

7. Additional Results

To conserve space in the main text, we here include several results additional from the coupled subsurface-atmospheric mixing model, as well as results examining parameter combinations within the candidate solution space.

7.1. Out-of-Phase Methane Variations

We observed that subsurface architectures with fracture density $\leq 0.005\%$ produced seasonal methane variations that were out of phase with the SAM-TLS observations. We here include the "best" scenarios associated with of these fracture density cases.

7.2. Seasonal Methane Variation

7.2.1. Fracture Density 0.02% and 0.035%

Other subsurface fracture cases that performed well were 0.035% (Figure S18) and 0.02% (Figure S17) fracture density, in that order. Compared to 0.01% fracture density, both of these higher fracture density cases better match the abundance observations in Northern Spring (L_s 0-90°). These cases also tended to better capture the increase in methane abundance that seems to occur in Northern Winter (L_s 270-360°), especially the case with fracture density 0.035%. That being said, methane abundance in these higher fracture density cases tends to fall off quicker as Northern Summer transitions into Northern Autumn, generally underpredicting methane concentrations relative to the apparent gradual decline in methane observed. The rapid fall-off is less pronounced for fracture density 0.02% versus 0.035%, which can be seen when comparing the fit to the SAM-TLS observation at $L_s = 189.2°$.

7.3. Sub-diurnal Methane Variation

7.3.1. Fracture Density 0.02% and 0.035%

Fracture networks that are less sparse (e.g., fracture density 0.02 and 0.035%, which compared to the 0.01% case have 2 and 3.5 times greater volume of fractures, respectively) produce flux patterns that are more diffuse (Figures S20f, S19f). The surface emissions in such cases are characterized by more frequent pulses of methane because transport through individual fracture pathways is less important than the overall contribution of multiple connected pathways. The resulting atmospheric abundances are, likewise, necessarily different than for cases with more sparse fracture networks (Figures S19, S20).

For fracture density 0.02%, smaller values of D_c (≤ 0.2 m^2 s^{-1}) better matched the inferred diurnal abundance variation. Such scenarios were in general agreement with SAM-TLS observations, with the exception of the intermediate positive detection on L_s 126.3° (at 23:56 LMST) mentioned in the previous section. Early-evening methane (17:00 - 21:00) pulses at certain L_s create methane abundance spikes that tend to quickly decay to background as the evening progresses. It is worth noting that the candidate parameter space for this fracture case was relatively small with regard to the range of D_c ($0.06 < D_c < 1.2$).

For fracture density 0.035%, larger values of D_c (≥ 1 m^2 s^{-1}) tended to better match the inferred diurnal abundance variation, though this relationship was not firm, as evidence by scenario c. As above, however, it is worth noting that the candidate parameter space for this fracture case was relatively small with regard to the range of D_c ($0.10 < D_c < 1.4$). In terms of surface methane flux, the majority of mass emitted occurs mid-sol, between the hours of 10:00 and 17:00 LMST (Figure S20f). A rising limb of methane abundance culminating in a sharp "lip" occurs just prior to PBL expansion due to a late morning methane flux pulse. There is also a smaller, less pronounced lip and falling limb that occurs just after PBL collapse, which is primarily due a sharp methane pulse occurring at that time. The lip and falling limb is due to this pulse and not because the bulk of methane is emitted mid-sol during the expanded PBL state, as evidenced by the late-season abundance ($L_s = 156.3°$), which has no corresponding pulse and likewise, no early-evening falling limb.

7.4. Analysis of Candidate Parameter Space

We further interrogated the candidate solution parameter space generated by the differential evolution optimization algorithm in order to understand the interaction between atmospheric mixing parameters, with results below. We analyzed the parameter space for fracture density cases where the overall χ^2_ν for the "best" set of parameters was less than 4.0. This choice of error value was somewhat arbitrarily chosen, as it appeared to be the cutoff error, over which the seasonal abundance variations were out of phase with the observations. This cutoff thereby limited the best fracture densities to 0.01%, 0.02%, and 0.035%. Candidate solutions in each case were populated from the results of the differential evolution optimization by including results with error $\chi^2_\nu \leq \min \chi^2_\nu + 0.5$ – this defines the "candidate solution parameter space".

7.4.1. Fracture Density 0.01%

The entire candidate solution parameter space is shown in Figure S21. Diffusion coefficients D_c and D_e, unsurprisingly, are correlated such that smaller D_c begets a smaller D_e. The candidate solution space contains diffusion coefficient values such that range of the ratio D_e/D_c is between 59 and 678 (Figure S22), with a mean value of 351. We initially provided bounds to the algorithm for this ratio of $1 \leq D_e/D_c \leq 1000$, so the atmospheric mixing model apparently favors comparatively large daytime eddy diffusivities compared to those during the collapsed state, although the absolute magnitudes of these diffusivities do not overly affect the results. A linear regression on $D_e = f(D_c)$ yields a slope of 10.8, with an adjusted R^2 value of 0.85. Also unsurprisingly, first-order methane loss terms k_c and k_e are inversely correlated in order to preserve mass balance in time. The range in the ratio of k_e/k_c is 1.01 to 3.21 having mean value 1.46, with the overall best scenarios in terms of error coming out of ratios close to unity. A linear regression on $k_e = f(k_c)$ yields a slope of -1.1, with an adjusted R^2 value of 0.67.

7.4.2. Fracture Density 0.02%

The candidate solution space contains diffusion coefficient values such that range of the ratio of D_e/D_c is between 848 and 873 (Figure S24), with a mean value of 862. A linear regression on $D_e = f(D_c)$ yields a slope of 9.91, with an adjusted R^2 value of 1.00. The range in the ratio of k_e/k_c is 1.00 to 1.52 having mean value 1.12, with the overall best scenarios in terms of error coming out of ratios close to unity. First-order methane loss terms k_c and k_e do not have a clear linear correlation.

7.4.3. Fracture Density 0.035%

The candidate solution space for the case where fracture density is 0.035% contains diffusion coefficient values such that range of the ratio D_e/D_c is between 469 and 994 (Figure S26), with a mean value of 729. We initially provided bounds to the algorithm for this ratio of $1 \leq D_e/D_c \leq 1000$, so the atmospheric mixing model apparently favors comparatively large daytime eddy diffusivities compared to those during the collapsed state. A linear regression on $D_e = f(D_c)$ yields a slope of 9.5, with an adjusted R^2 value of 0.95. Also unsurprisingly, first-order methane loss terms k_c and k_e are inversely correlated (though to a lesser degree than in the fracture density 0.01$ case) in order to preserve mass balance in time. The range in the ratio of k_e/k_c is 1.02 to 1.66, having mean value 1.22, with the overall best scenarios in terms of error coming out of ratios close to unity. A linear regression on $k_e = f(k_c)$ yields a slope of -0.48, with an adjusted R^2 value of 0.27.

References

Adobe Inc. (2019). *Adobe Illustrator.* [Software]. Retrieved from `https://adobe.com/products/illustrator`

Carslaw, H. S., & Jaeger, J. C. (1959). *Conduction of Heat in Solids* (2nd ed.). Oxford: Clarendon Press.

Clemo, T. M., & Smith, L. (1997). A hierarchical model for solute transport in fractured media. *Water Resources Research*, *33*(8), 1763–1783.

Cooley, J. W., & Tukey, J. W. (1965). An Algorithm for the Machine Calculation of Complex Fourier Series. *Mathematics of Computation*, *19*(90), 297–301. doi: 10.2307/2003354

Geier, J. E., Lee, K., & Dershowitz, W. S. (1988). Field validation of conceptual models for fracture geometry. *Transactions of American Geophysical Union*, *69*(44), 1177.

Gough, R. V., Tolbert, M. A., McKay, C. P., & Toon, O. B. (2010). Methane adsorption on a martian soil analog: An abiogenic explanation for methane variability in the martian atmosphere. *Icarus*, *207*(1), 165–174. Retrieved from `http://dx.doi.org/10.1016/j.icarus.2009.11.030` doi: 10.1016/j.icarus.2009.11.030

Harp, D. R., Ortiz, J. P., & Stauffer, P. H. (2019). Identification of dominant gas transport frequencies during barometric pumping of fractured rock. *Scientific Reports*, *9*(1), 9537. doi: 10.1038/s41598-019-46023-z

Jones, E. G., Lineweaver, C. H., & Clarke, J. D. (2011). An extensive phase space for the potential Martian biosphere. *Astrobiology*, *11*(10), 1017–1033. doi: 10.1089/ast.2011.0660

Kronyak, R. E., Kah, L. C., Edgett, K. S., VanBommel, S. J., Thompson, L. M., Wiens, R. C., ... Nachon, M. (2019). Mineral-Filled Fractures as Indicators of Multigenerational Fluid Flow in the Pahrump Hills Member of the Murray Formation, Gale Crater, Mars. *Earth and Space Science*, *6*(2), 238–265. doi: 10.1029/2018EA000482

Lin, J. T., & McElroy, M. B. (2010). Impacts of boundary layer mixing on pollutant vertical profiles in the lower troposphere: Implications to satellite remote sensing. *Atmospheric Environment*, *44*(14), 1726–1739. Retrieved from `http://dx.doi.org/10.1016/j.atmosenv.2010.02.009` doi: 10.1016/j.atmosenv.2010.02.009

Mellon, M. T., & Phillips, R. J. (2001). Recent gullies on Mars and the source of liquid water. *Journal of Geophysical Research E: Planets*, *106*(E10), 23165–23179. doi: 10.1029/2000JE001424

Meslin, P. Y., Gough, R., Lefvre, F., & Forget, F. (2011). Little variability of methane on Mars induced by adsorption in the regolith. *Planetary and Space Science*, *59*(2-3), 247–258. doi: 10.1016/j.pss.2010.09.022

Moores, J. E., Gough, R. V., Martinez, G. M., Meslin, P. Y., Smith, C. L., Atreya, S. K., ... Webster, C. R. (2019). Methane seasonal cycle at Gale Crater on Mars consistent with regolith adsorption and diffusion. *Nature Geoscience*, *12*(5), 321–325. doi: 10.1038/s41561-019-0313-y

Newman, C. E., Gómez-Elvira, J., Marin, M., Navarro, S., Torres, J., Richardson, M. I., ... Bridges, N. T. (2017). Winds measured by the Rover Environmental Monitoring Station (REMS) during the Mars Science Laboratory (MSL) rover's Bagnold Dunes Campaign and comparison with numerical modeling using MarsWRF. *Icarus*, *291*(December 2016), 203–231. Retrieved from `http://dx.doi.org/10.1016/j.icarus.2016.12.016` doi: 10.1016/j.icarus.2016.12.016

Newman, C. E., Kahanpää, H., Richardson, M. I., Martínez, G. M., Vicente-Retortillo, A., & Lemmon, M. T. (2019). MarsWRF Convective Vortex and Dust Devil Predictions for Gale Crater Over 3

Mars Years and Comparison With MSL-REMS Observations. *Journal of Geophysical Research: Planets*, *124*(12), 3442–3468. doi: 10.1029/2019JE006082

Nilson, R. H., Peterson, E. W., Lie, K. H., Burkhard, N. R., & Hearst, J. R. (1991). Atmospheric Pumping: A Mechanism Causing Vertical Transport of Contaminated Gases Through Fractured Permeable Media. *Journal of Geophysical Research: Solid Earth*, *96*(B13), 933–948. doi: 10.2752/147597509112541

Ordonez-Etxeberria, I., Hueso, R., & Sánchez-Lavega, A. (2018). A systematic search of sudden pressure drops on Gale crater during two Martian years derived from MSL/REMS data. *Icarus*, *299*, 308–330. doi: 10.1016/j.icarus.2017.07.032

Ordóñez-Etxeberria, I., Hueso, R., & Sánchez-Lavega, A. (2020). Strong increase in dust devil activity at Gale crater on the third year of the MSL mission and suppression during the 2018 Global Dust Storm. *Icarus*, *347*(February). doi: 10.1016/j.icarus.2020.113814

Ortiz, J. P., Rajaram, H., Stauffer, P. H., Harp, D. R., Wiens, R. C., & Lewis, K. W. (2022). [SI] Barometric Pumping Through Fractured Rock: A Mechanism for Venting Deep Methane to Mars' Atmosphere. *Geophysical Research Letters*, *49*(14), 1–25. doi: 10.1029/2022GL098946

Richardson, M. I., Toigo, A. D., & Newman, C. E. (2007). PlanetWRF: A general purpose , local to global numerical model for planetary atmospheric and climate dynamics. *Journal of Geophysical Research*, *112*(E9), 1–29. doi: 10.1029/2006JE002825

Storn, R., & Price, K. (1997). Differential Evolution – A Simple and Efficient Heuristic for global Optimization over Continuous Spaces. *Journal of Global Optimization*, *11*(4), 341–359. Retrieved from `http://dx.doi.org/10.1023/A:1008202821328` doi: 10.1023/A:1008202821328

Viswanathan, G. M., Buldyrev, S. V., Havlin, S., Da Luz, M. G., Raposo, E. P., & Stanley, H. E. (1999). Optimizing the success of random searches. *Nature*, *401*(6756), 911–914. doi: 10.1038/44831

Webster, C. R., Mahaffy, P. R., Atreya, S. K., Moores, J. E., Flesch, G. J., Malespin, C., ... Navarro-Gonzalez, R. (2018a). Background levels of methane in Mars' atmosphere show strong seasonal variations. *Science*, *360*(6393), 1093–1096.

Webster, C. R., Mahaffy, P. R., Atreya, S. K., Moores, J. E., Flesch, G. J., Malespin, C., ... Vasavada, A. R. (2018b). [Supplementary Material] Background levels of methane in Mars' atmosphere show strong seasonal variations. *Science*, *360*(6393), 1093–1096. doi: 10.1126/science.aaq0131

Webster, C. R., Mahaffy, P. R., Pla-Garcia, J., Rafkin, S. C., Moores, J. E., Atreya, S. K., ... Vasavada, A. R. (2021). Day-night differences in Mars methane suggest nighttime containment at Gale crater. *Astronomy and Astrophysics*, *650*(December 2019), 1–14. doi: 10.1051/0004-6361/202040030

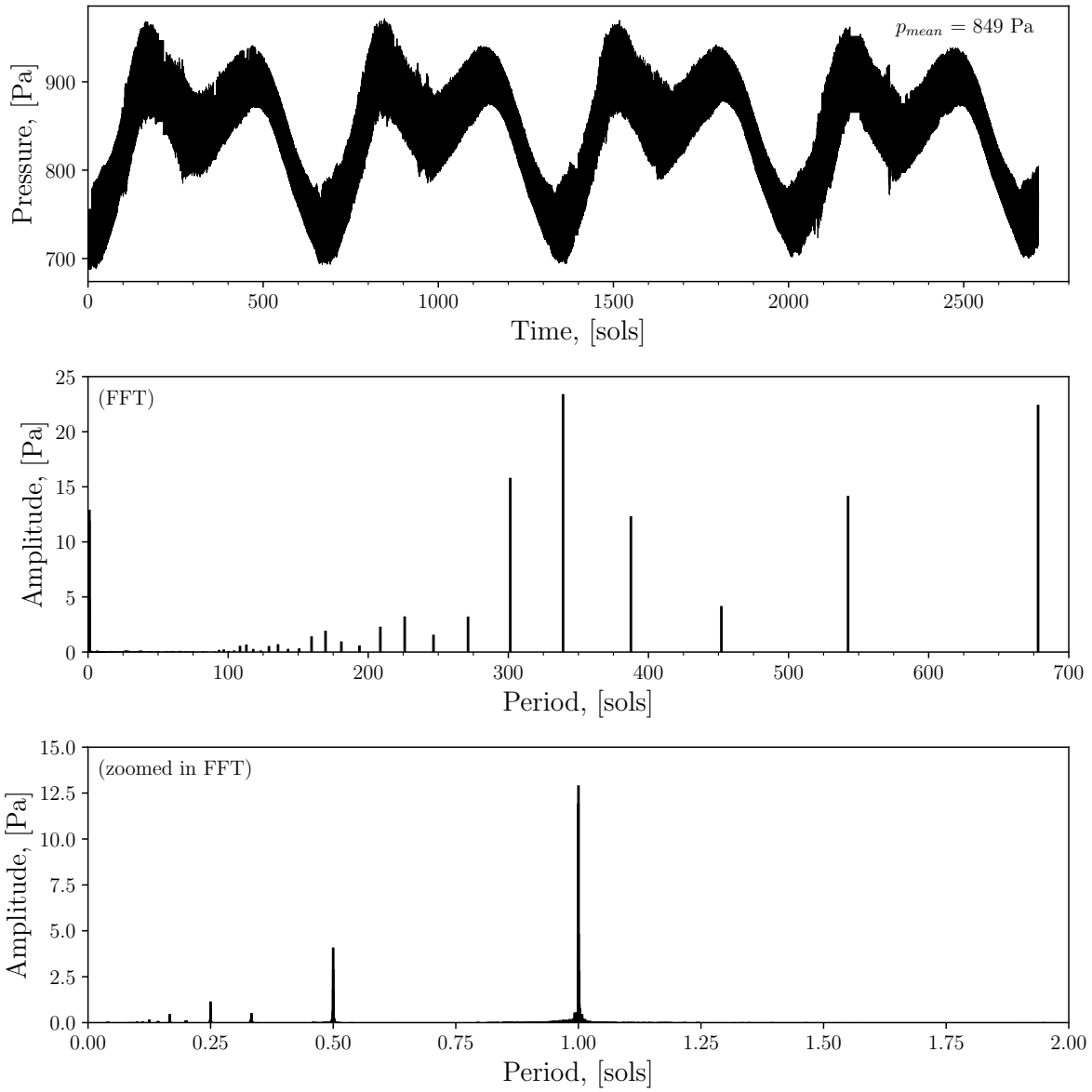

Figure S1. Spectral decomposition of the elevation-corrected barometric pressure data collected by *Curiosity* rover through mission sol 2713: (top) barometric record time series with data gaps filled using the procedure outlined previously; (middle) spectral decomposition of the barometric record into its associated amplitude/period pairs, showing the relative strength of each periodic component; (bottom) zoomed in portion of the spectral decomposition to highlight the roughly diurnal barometric component.

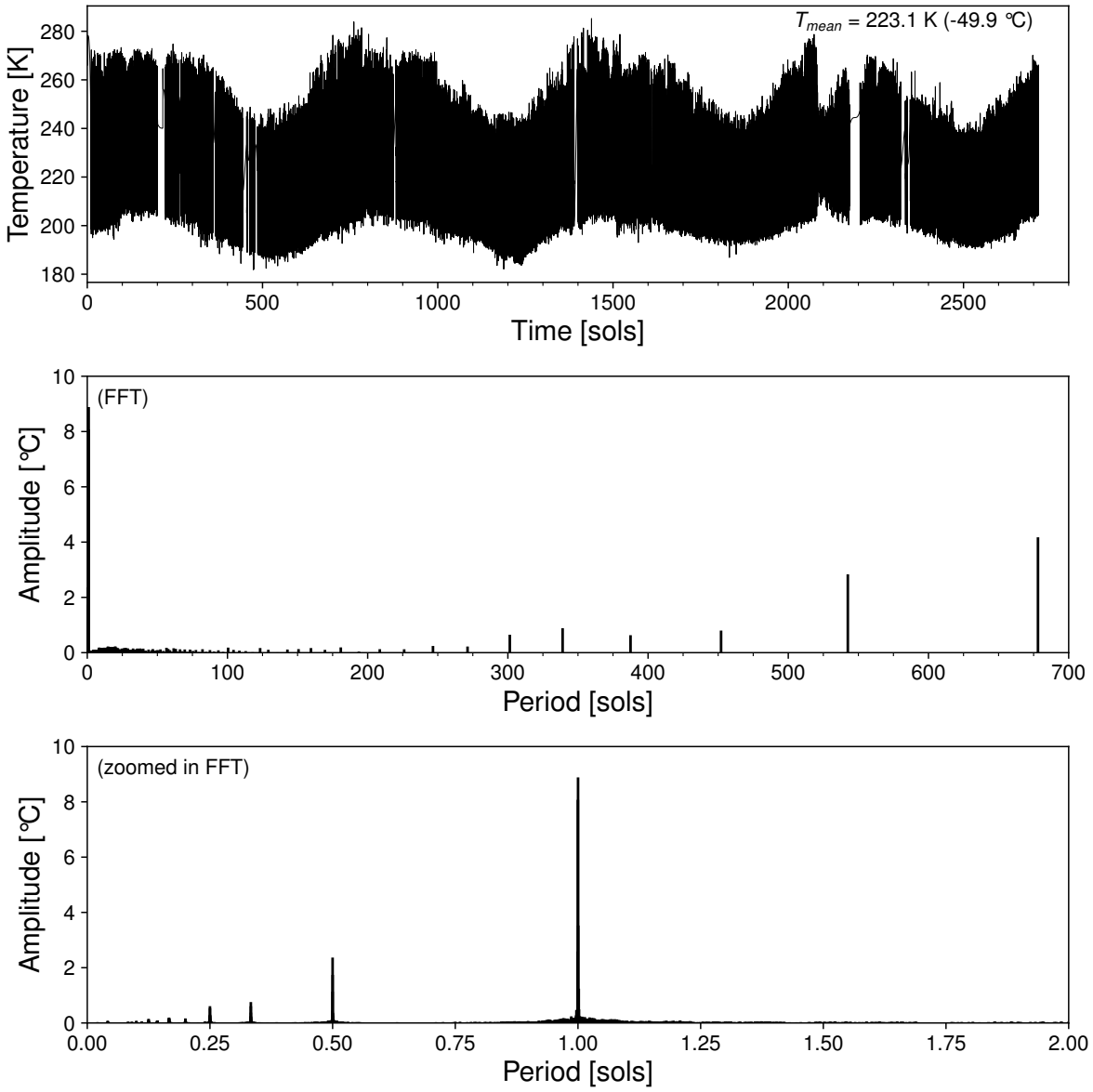

Figure S2. Spectral decomposition of the ambient temperature data collected by *Curiosity*: (top) temperature record time series; (middle) spectral decomposition of the temperature record into its associated amplitude/period pairs, showing the relative strength of each periodic component; (bottom) zoomed in portion of the spectral decomposition to highlight the roughly diurnal temperature component.

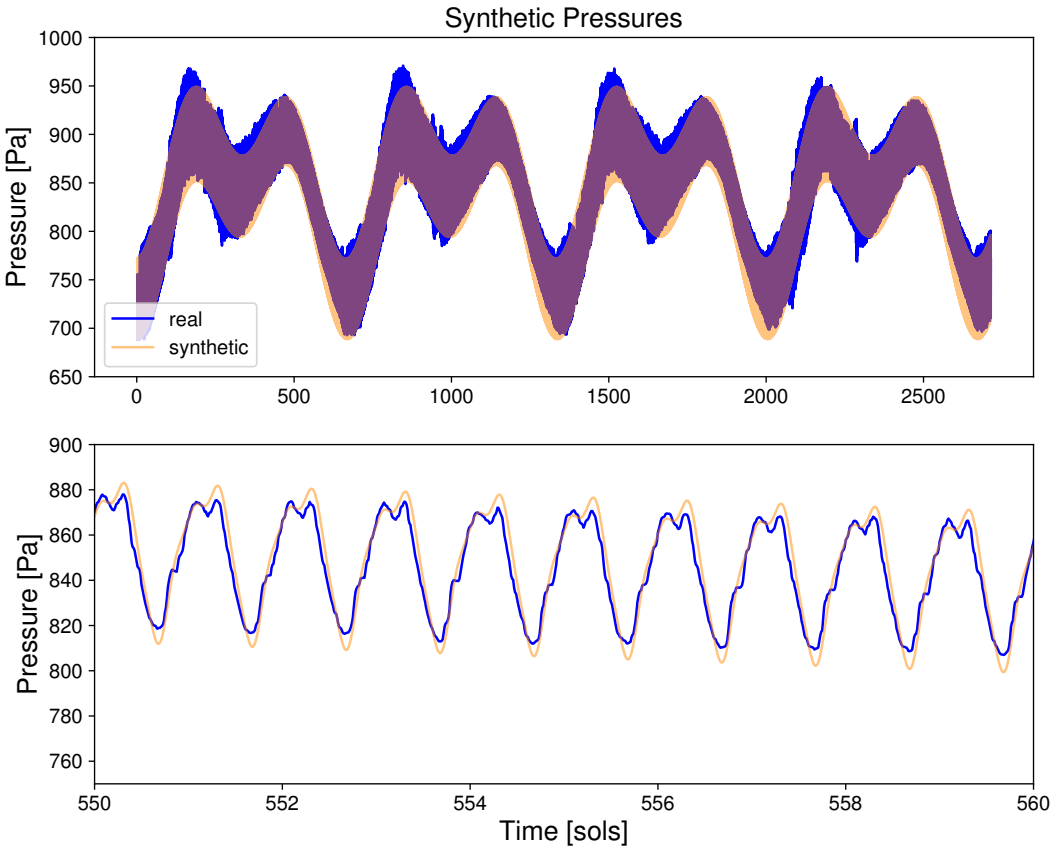

Figure S3. Generated synthetic pressures compared to elevation-corrected observed pressures for the first four Mars years of the MSL mission. (Top) The 1-year synthetic pressures repeated to match the extent of the observed pressures. (Bottom) Zooming in on a 10-sol segment of the barometric record to illustrate diurnal variations.

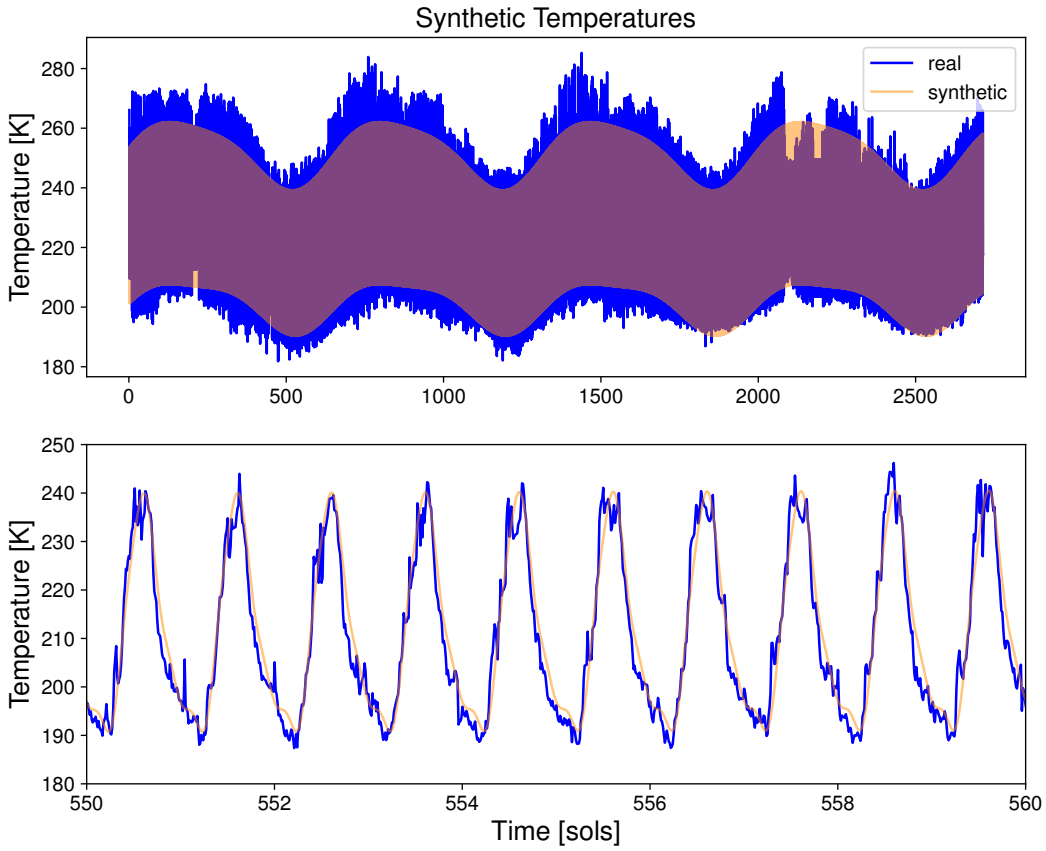

Figure S4. Generated synthetic surface temperatures compared to observed temperatures for the first four Mars years of the MSL mission. (Top) The 1-year synthetic temperatures repeated to match the extent of the observed temperatures. (Bottom) Zooming in on a 10-sol segment of the barometric record to illustrate diurnal variations.

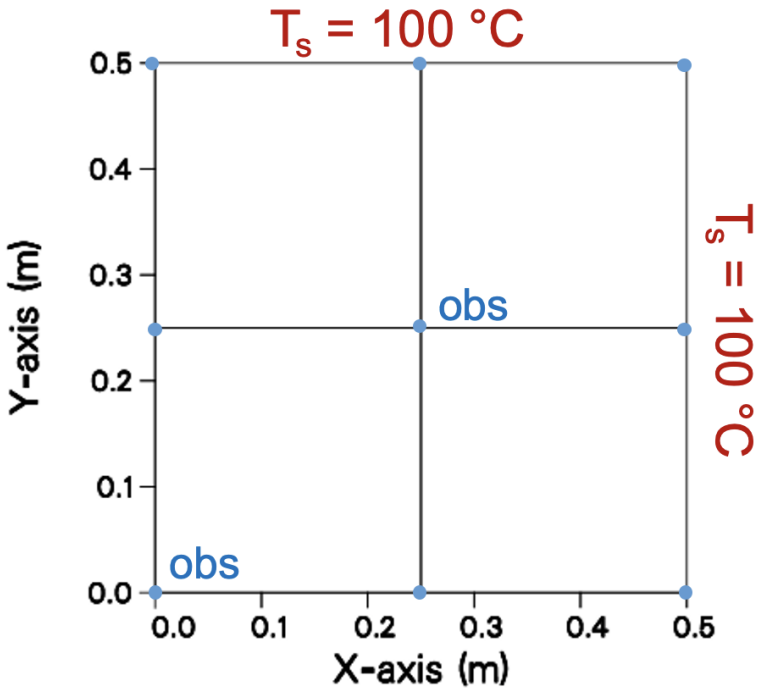

Figure S5. Schematic of the simple heat conduction verification problem set up in FEHM.

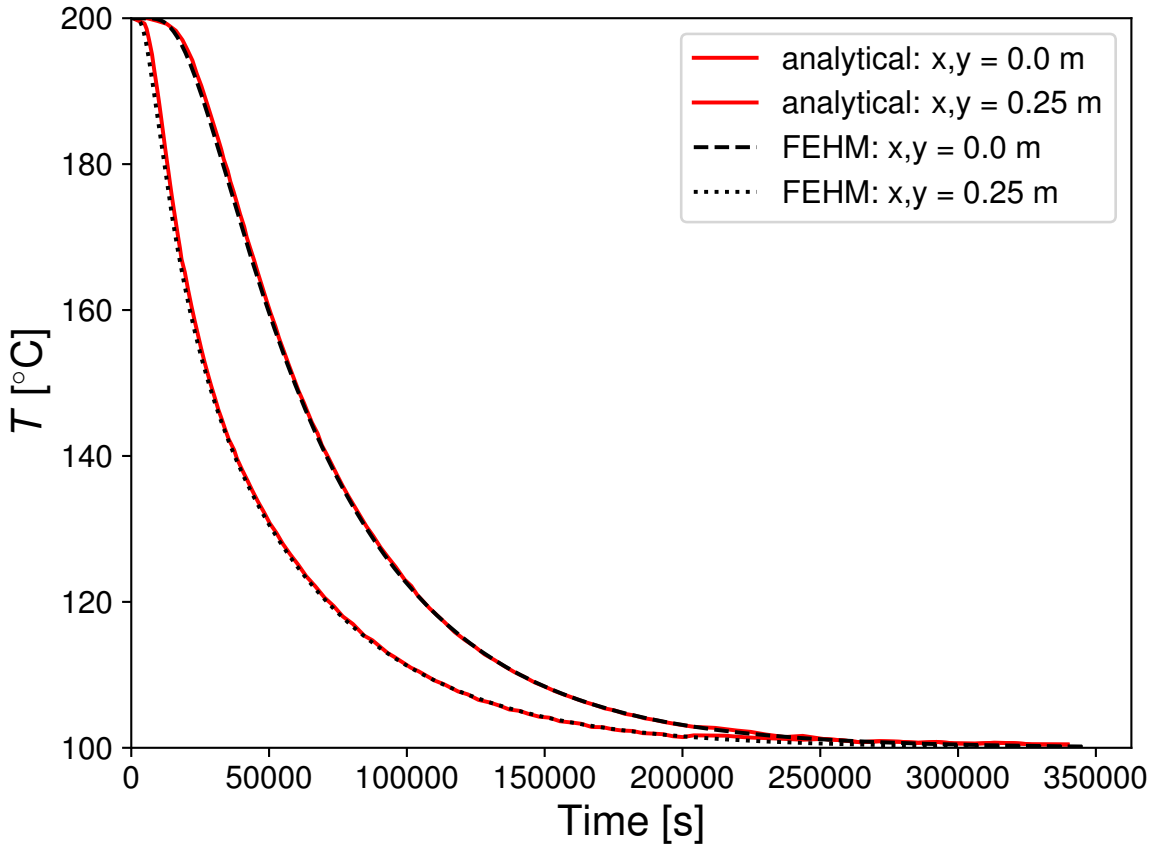

Figure S6. Results of the simulated simple heat conduction verification problem compared to the corresponding analytical solution.

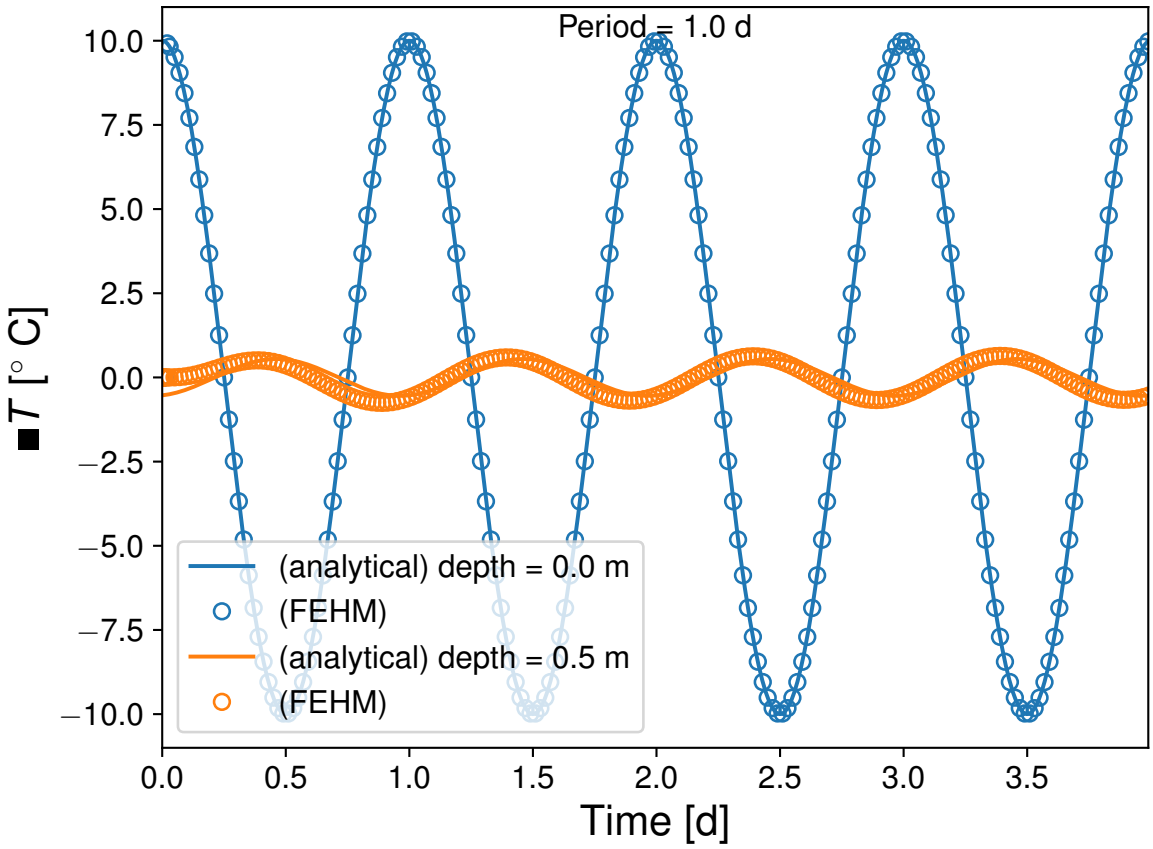

Figure S7. Comparison of simulated to analytical subsurface oscillatory thermal wave propagation.

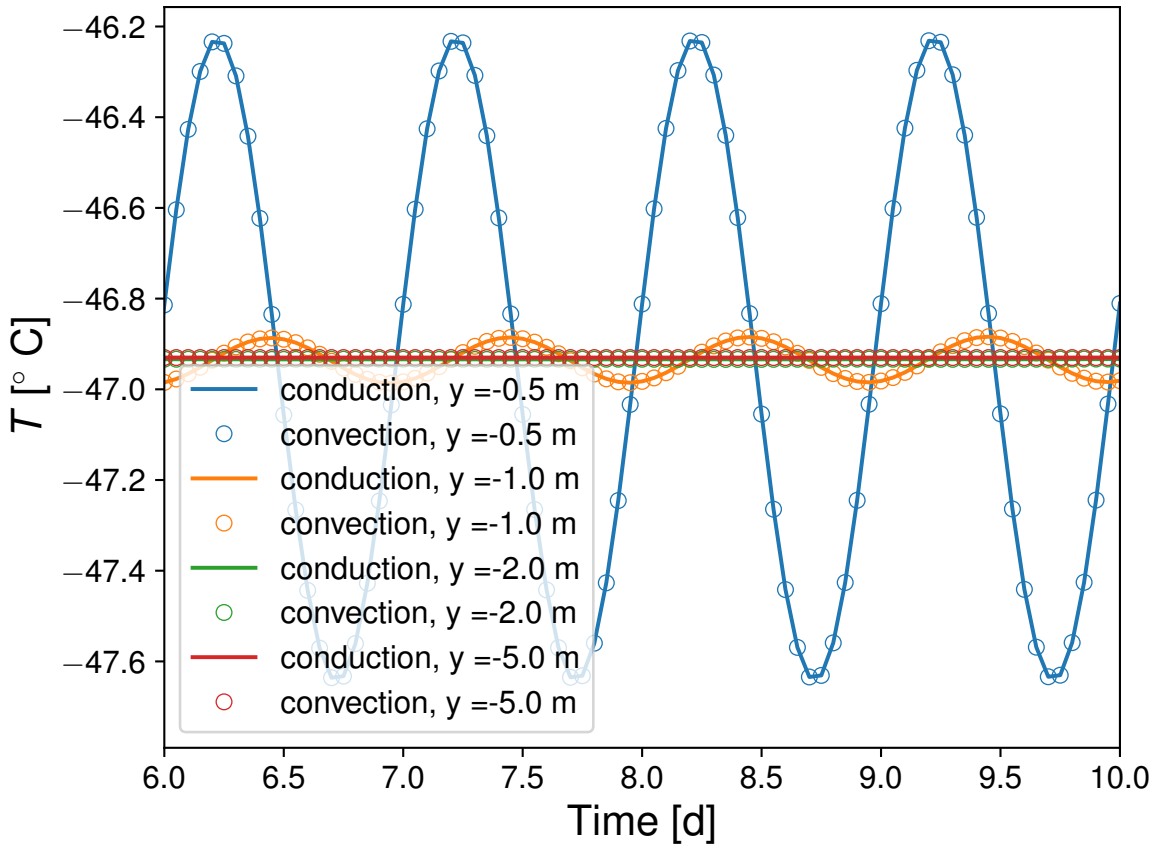

Figure S8. Comparison of subsurface temperature oscillations in purely conductive and conductive-convective regimes. The difference in subsurface temperatures is negligible due to the low density of CO_2 gas in Mars' atmosphere.

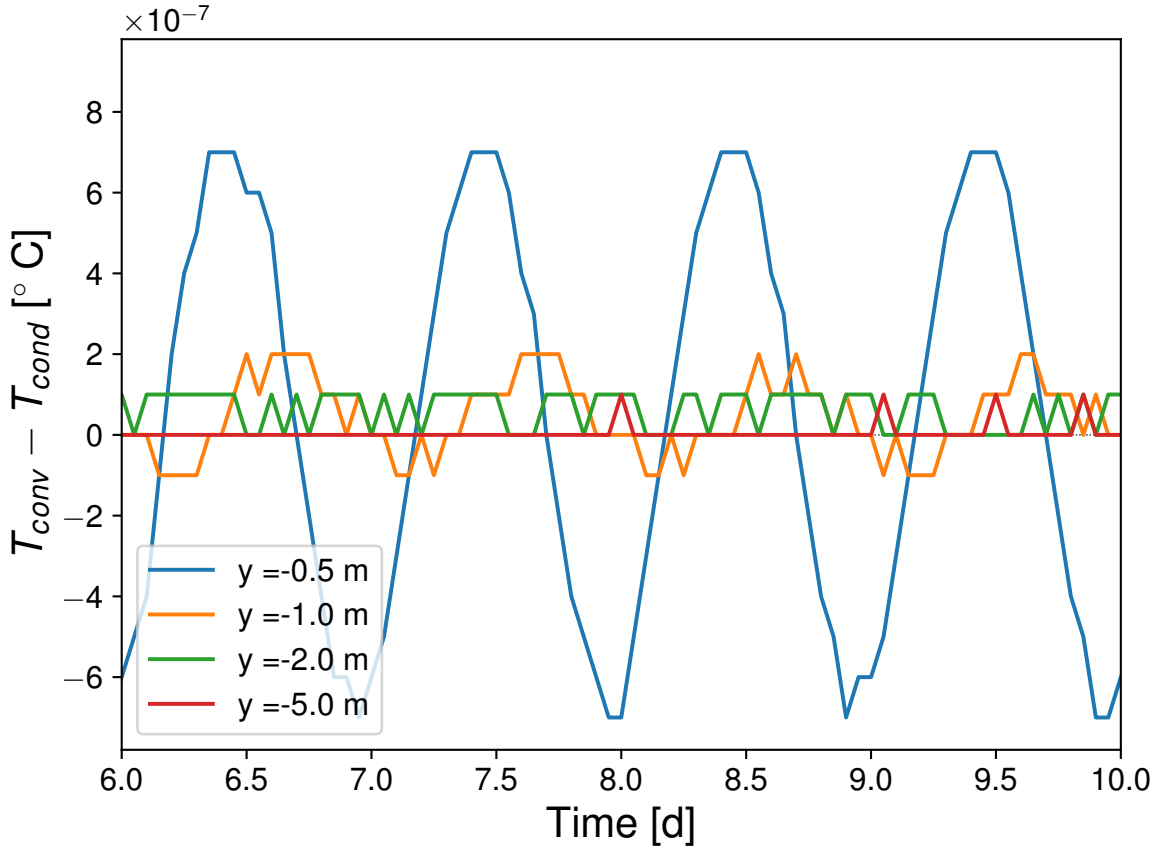

Figure S9. Difference between subsurface temperatures in time for convective and conductive heat flow using diurnal forcing. Results indicate very small differences in temperatures.

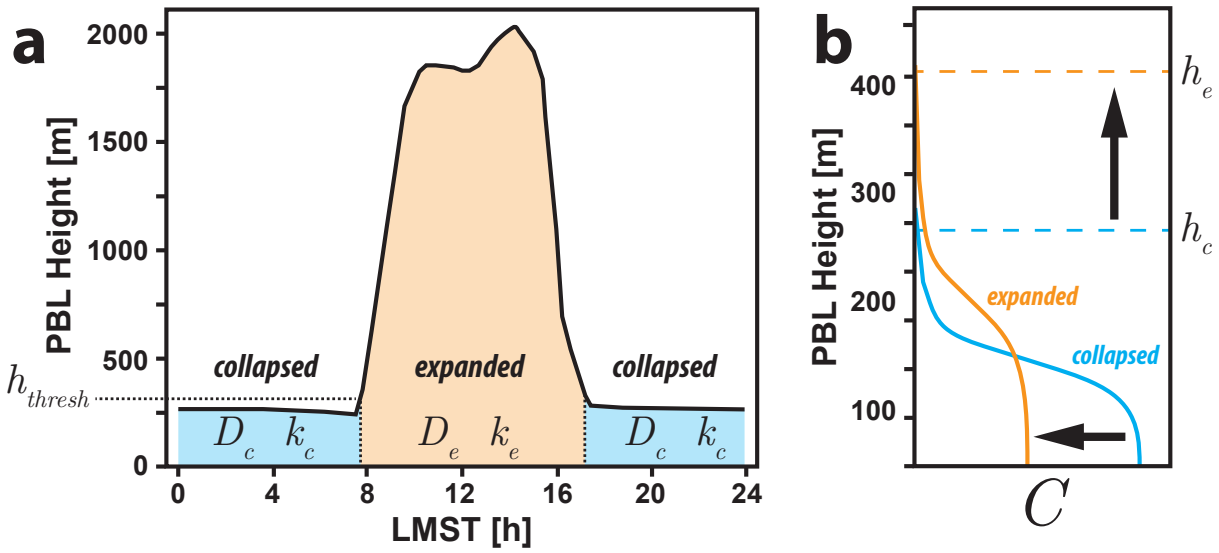

Figure S10. Schematic of the implementation of the diffusive atmospheric mixing model. (a) Delineation of the modeled atmospheric transport variables D_n and k_n based on PBL state change, where subscript n represents either c or e to indicate collapsed or expanded PBL states, respectively. PBL time series shown is representative of N. Summer, and varies throughout the Mars year in 30° L_s increments according to Newman et al. (2017). Transition from collapsed to expanded-state conditions is demarcated by PBL height cross threshold column height h_{thresh}. (b) Illustration showing the transition of initial state of the vertical concentration profile $C(z)$ in the model for an expanding PBL column (i.e., going from collapsed to expanded state). Total CH_4 mass in the atmospheric column is conserved during this transition.

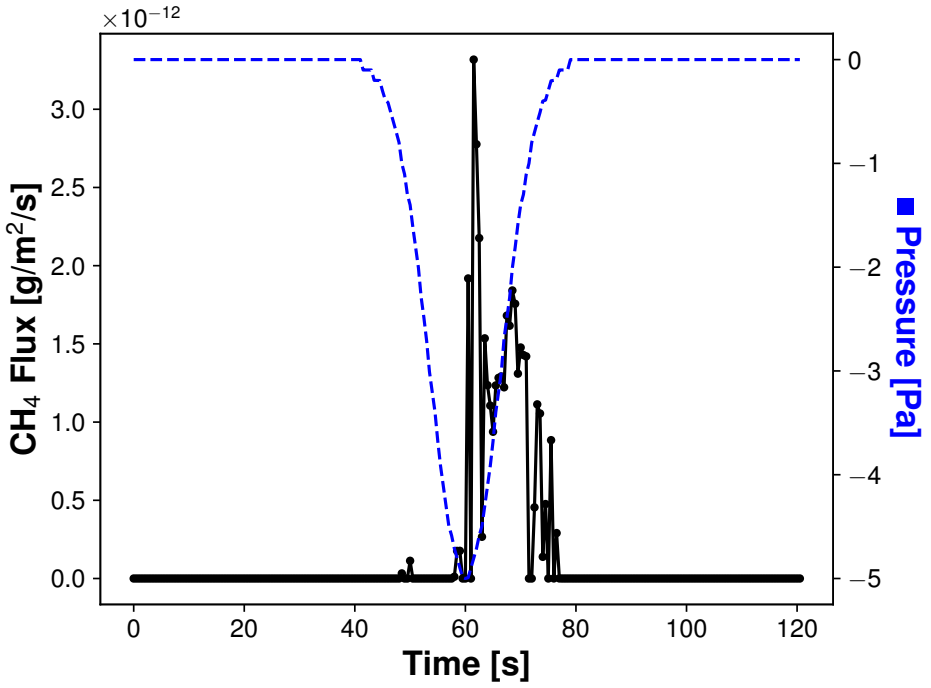

Figure S11. Surface methane fluxes induced by a large dust devil detected by MSL-REMS. Duration of the pressure drop was 25 s, with a drop in pressure (ΔP) of 5 Pa.

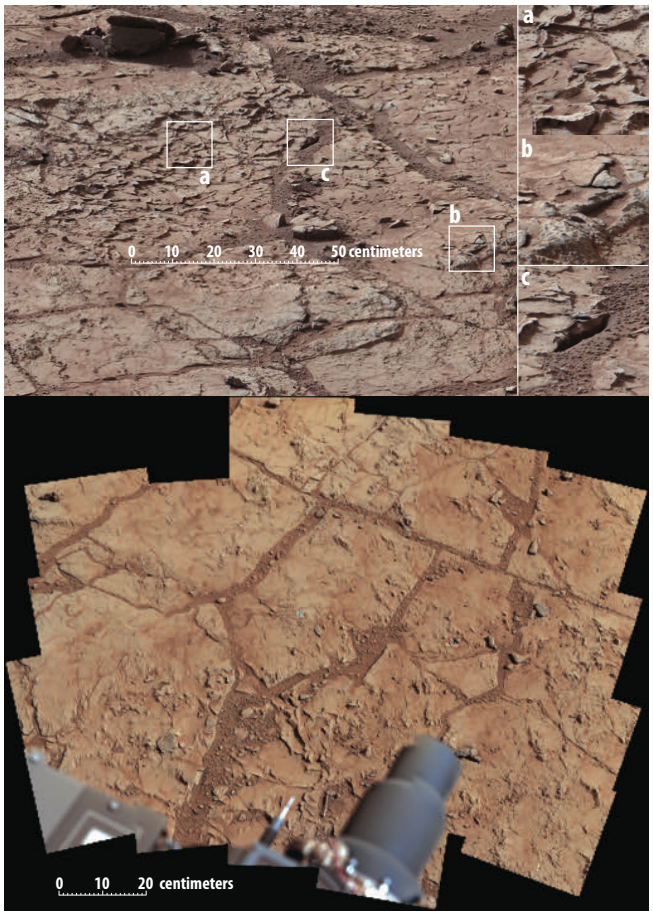

Figure S12. Examples of macroscopic surface fractures at Gale crater photographed by *Curiosity*'s Mastcam. (Top) A view of a patch of veined, flat-lying rock selected as the first drilling site for *Curiosity*, taken on sol 153 in the Yellowknife Bay geologic formation. Three boxes, each about 10 cm across, designate enlargements illustrating attributes of the area: (a) a high concentration of ridge-like veins protruding above the surface, with some veins having two walls and an eroded interior; (b) a horizontal discontinuity a few centimeters beneath the surface, which may be a bed, a fracture, or a horizontal vein; (c) a hole developed in the sand overlying a fracture, which implies a shallow infiltration of sand down into the fracture system. (Bottom) mosaic of the area, called "John Klein", where the rover performed its first sample drilling. Surface expression of these fractures show apertures on the scale of 1-2 cm, with most of the fracture volume occupied by unconsolidated material filling. Image credits: (top) NASA/JPL-Caltech/MSSS; (bottom) NASA/JPL-Caltech/MSSS.

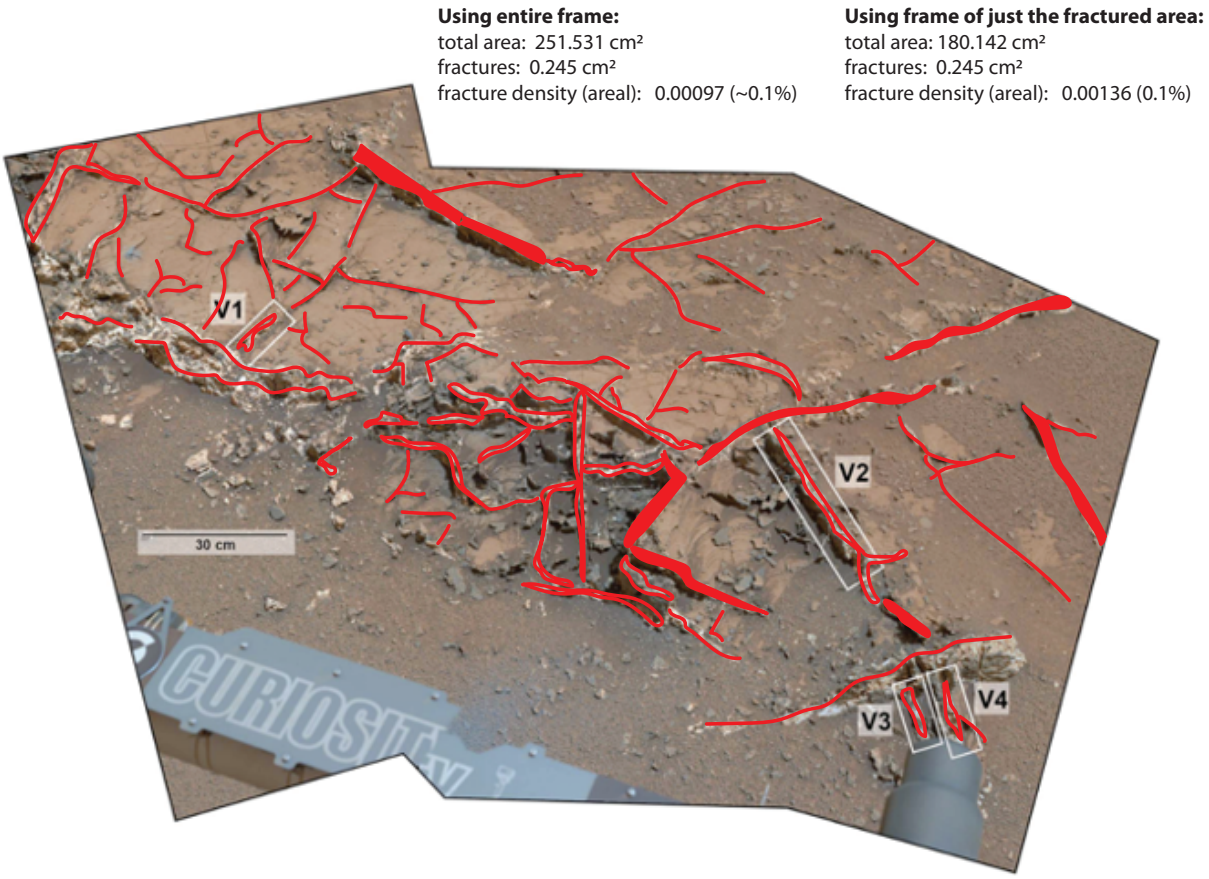

Figure S13. Fracture trace method used to approximate the areal "fracture density" of Mars' subsurface, applied to a Mastcam-34 mosaic (Kronyak et al., 2019) of the Garden City vein (mineral-filled fracture) complex at Gale crater. Centimeter-thick sandwich veins comprise the positive-relief intersecting network. Note that annotated areal dimensions are based on screen dimensions rather than the physical outcrop.

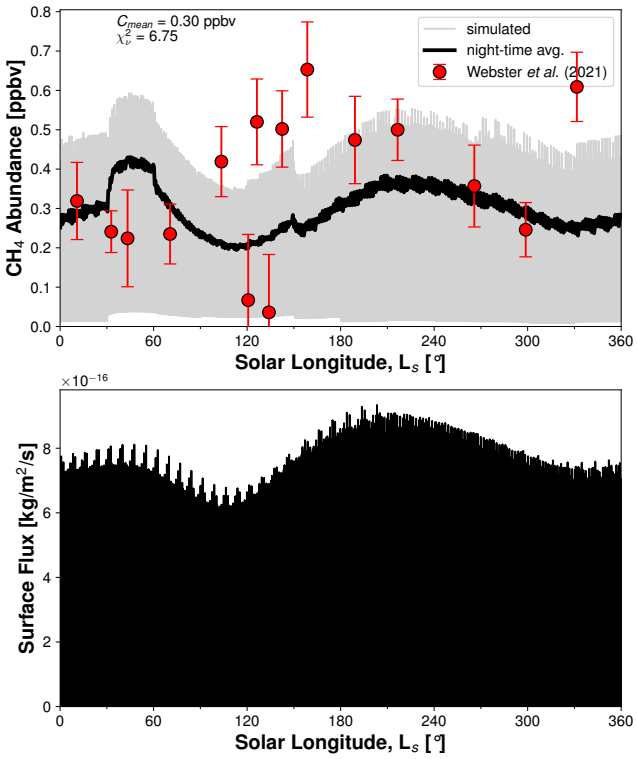

Figure S14. "Best" scenario atmospheric methane abundance and surface flux for scenario with fracture density 0.0%. (Top) Comparison of simulated (gray) to measured (circles) atmospheric methane abundance values plotted against solar longitude, L_s [°]. Night-time averages of the simulated abundance (thick black line) is plotted to aid visualization because of the large diurnal variations present (gray band). Measured abundances are from Webster et al. (2021). Note that some measurements were taken in different Mars years. (Bottom) Surface methane fluxes generated by barometric pumping over the same time period. These surface fluxes are input to the coupled atmospheric mixing model to generate the atmospheric mixing ratios above.

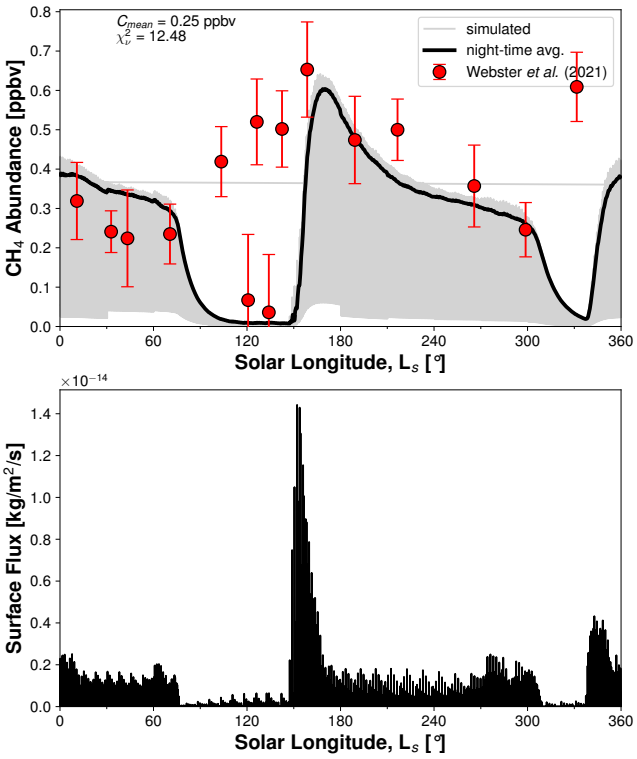

Figure S15. Same as Figure S14, but for fracture density 0.001%.

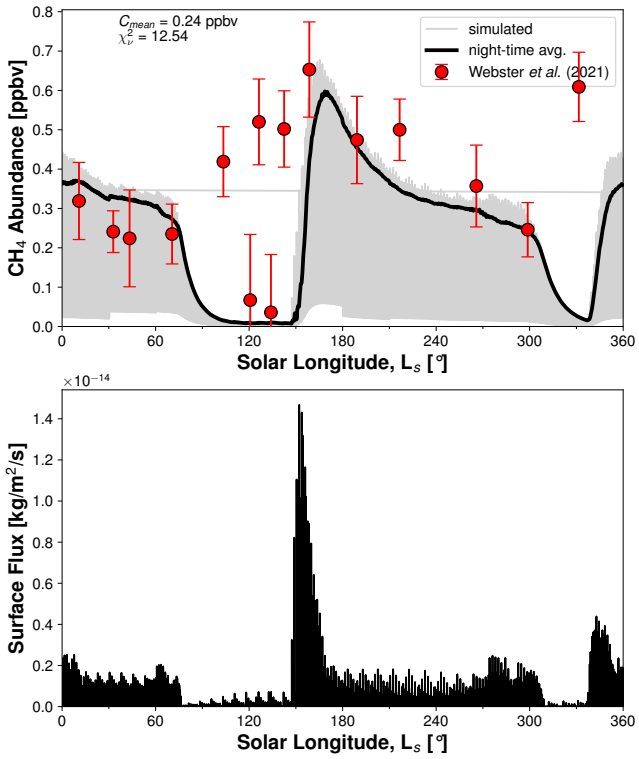

Figure S16. Same as Figure S14, but for fracture density 0.005%.

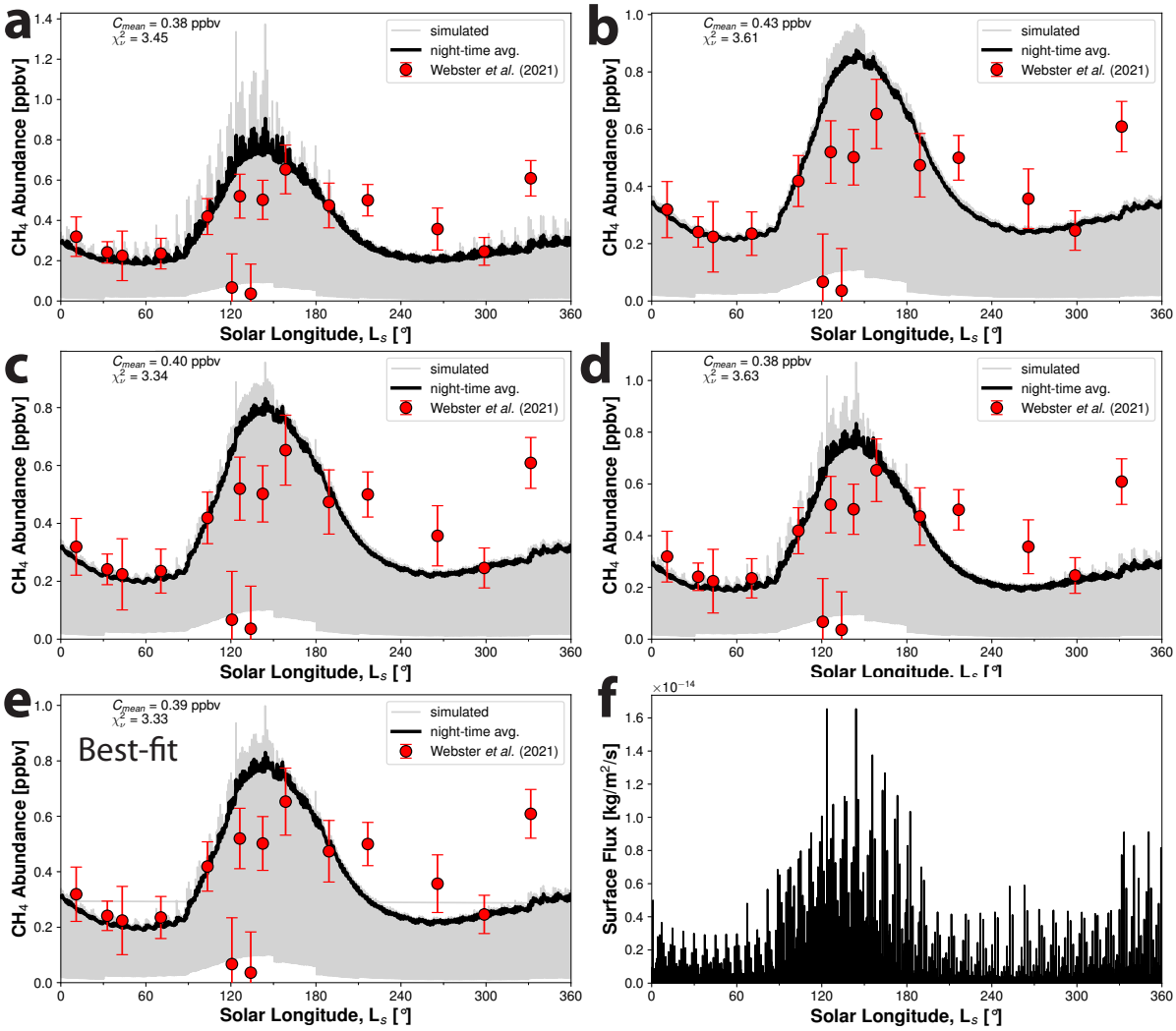

Figure S17. Composite of atmospheric methane abundance simulations for end-member scenarios analyzed for the case with fracture density 0.020%. Panel letters **a-d** correspond to lettering of atmospheric transport parameter end-member scenarios. Panel **e** is the "best" fitting scenario, and panel **f** is the surface methane flux. Comparison of simulated (gray) to measured (circles) atmospheric methane abundance values plotted against solar longitude, L_s [°]. Night-time averages of the simulated abundance (thick black line) is plotted to aid visualization because of the large diurnal variations present (gray band). Measured abundances are from Webster et al. (2021). Note that some measurements were collected in different Mars years.

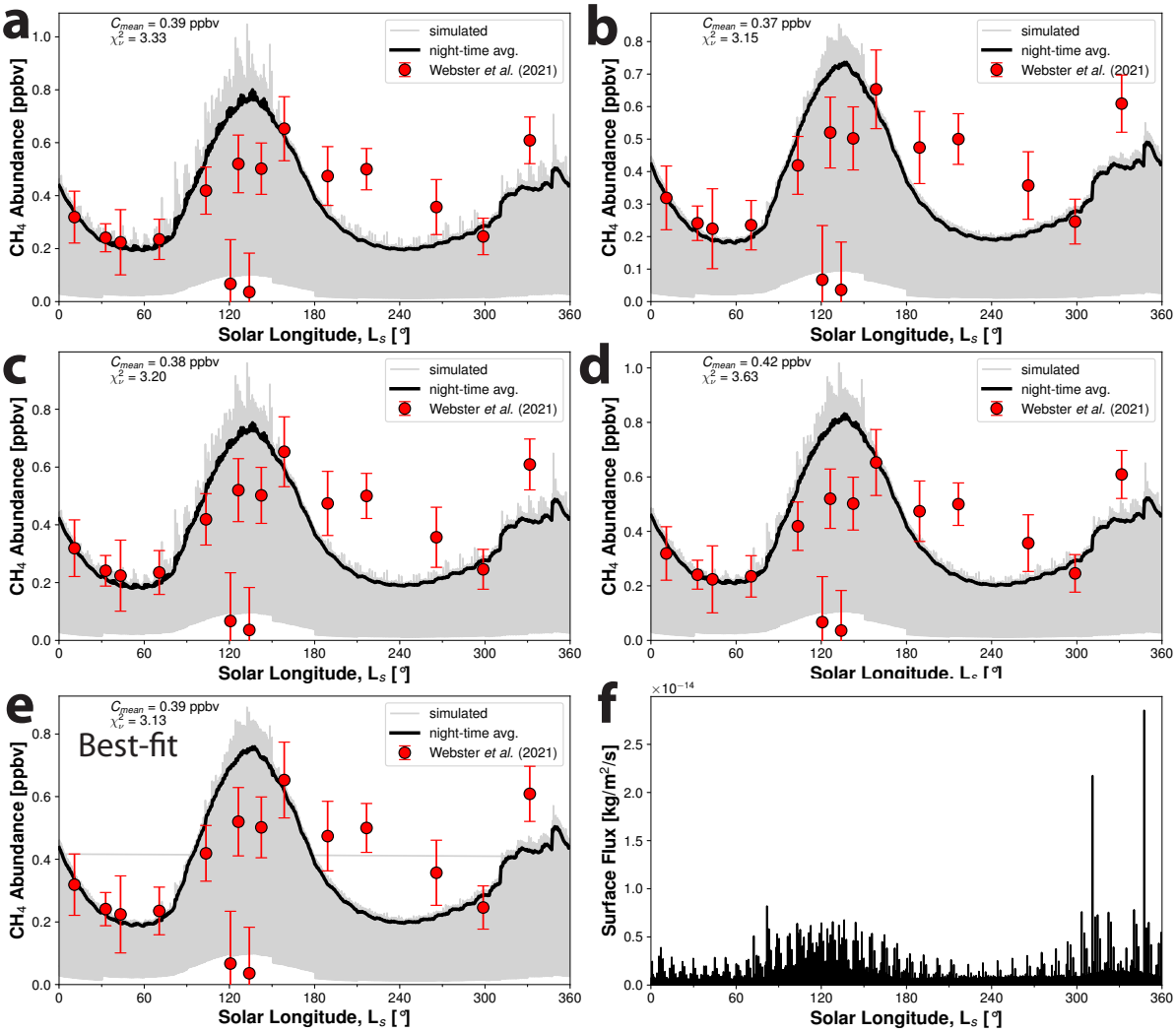

Figure S18. Same as in Figure S17, but for the case with fracture density 0.035%.

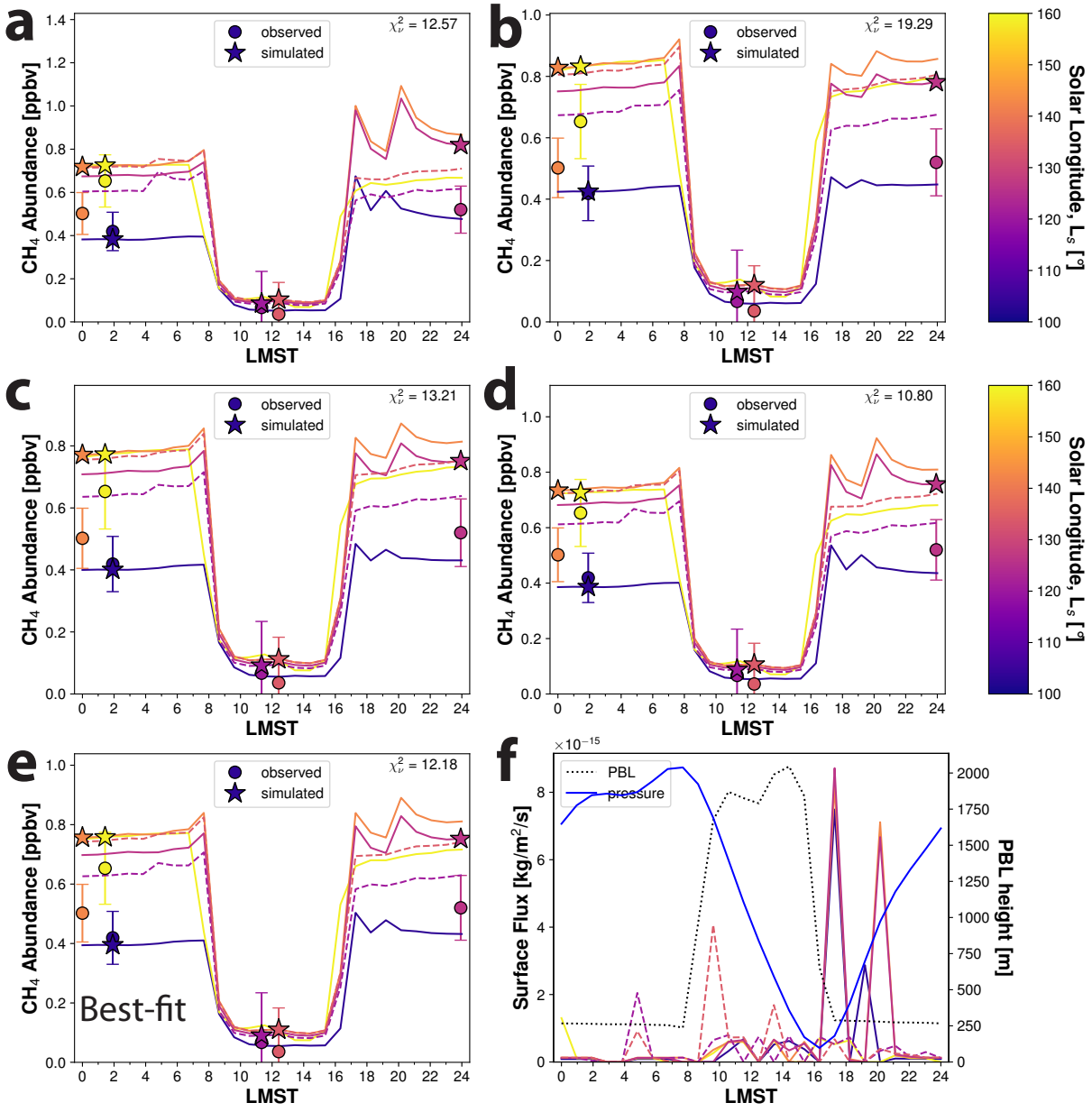

Figure S19. Composite of atmospheric mixing end-member scenarios simulating atmospheric methane abundance for the case with fracture density 0.020%. Panels **a-e** compare simulated (stars, lines) to measured (circles) atmospheric abundance values in local time, LMST, for Northern Summer, which highlights the day-night difference in abundance largely caused by the elevated planetary boundary layer (PBL) height h_{PBL}. Simulated abundances of the sols with non-detections are indicated by dashed lines. Measured abundances from Webster et al. (2021). Note that all measurements were taken on different sols and, in some cases, different Mars years, with the solar longitude, L_s [°] of the measurement indicated on the plot by its color. Panel letters **a-d** correspond to lettering of end-member scenarios. Panel **e** is the "best" fitting scenario, and panel **f** is the surface methane flux. Surface flux in local time (solid and dashed lines as above) plotted

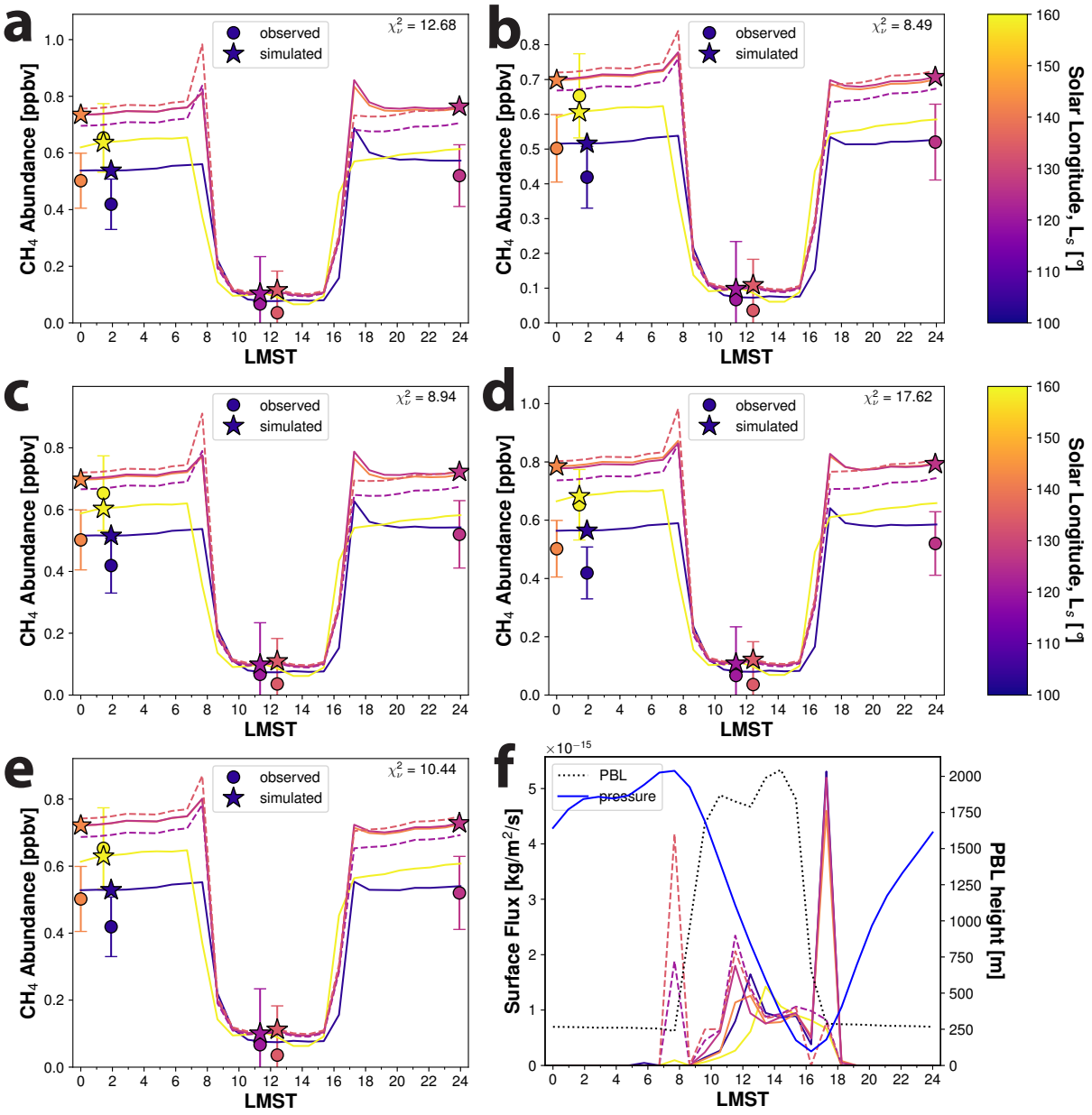

Figure S20. Same as in Figure S19, but for the case with fracture density 0.035%.

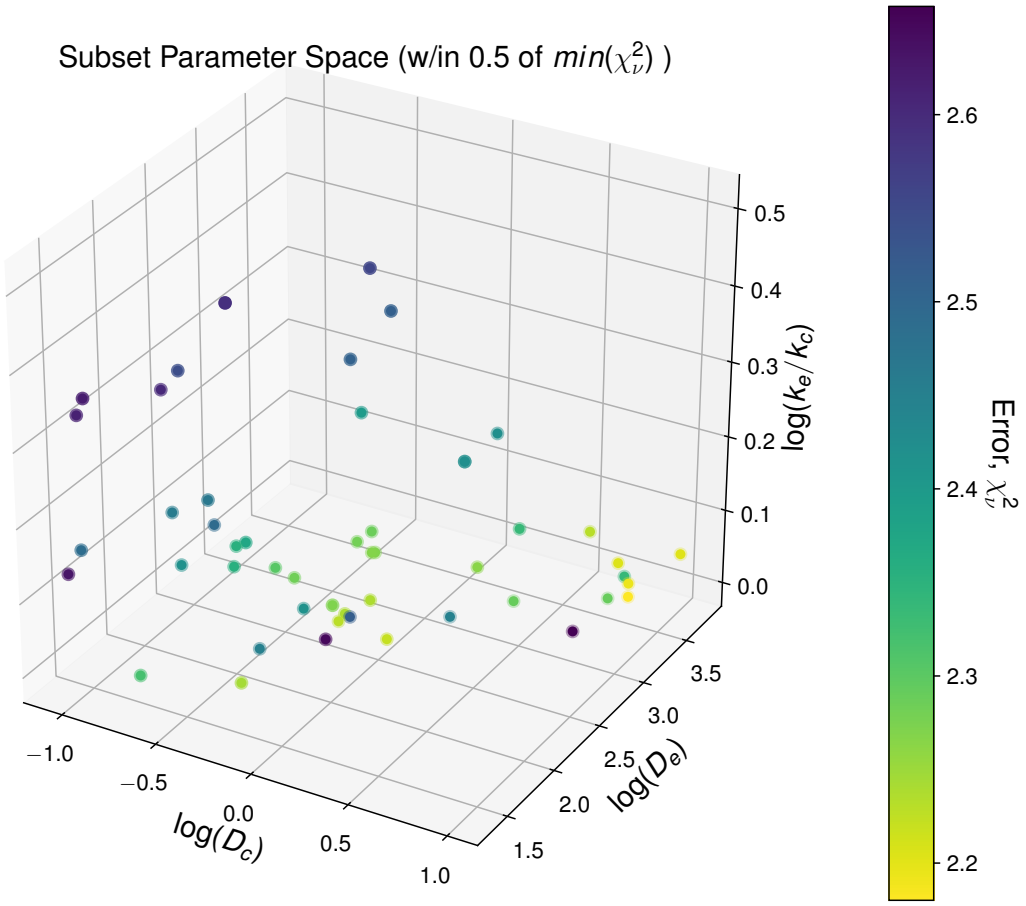

Figure S21. Candidate solution parameter space for the case with fracture density 0.010%.

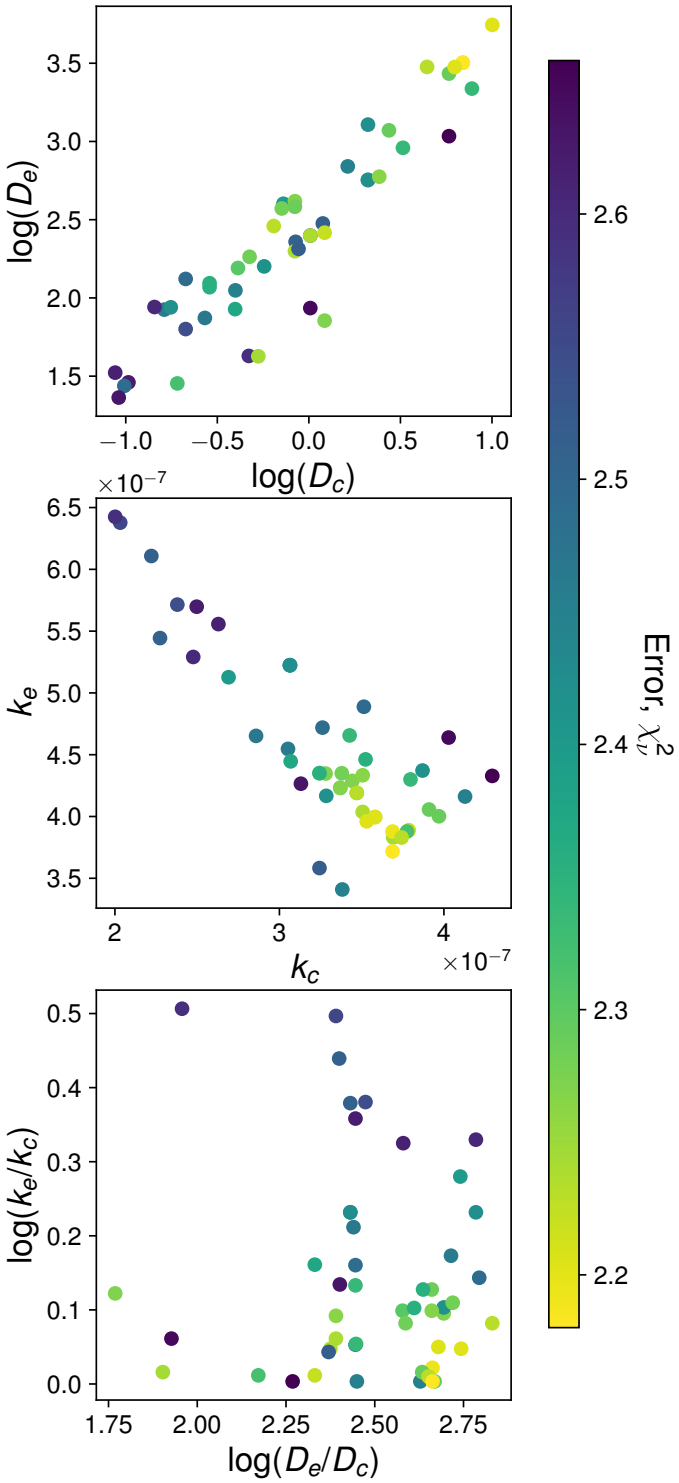

Figure S22. Comparison of individual atmospheric mixing parameters within the candidate solution parameter space for fracture density 0.010%.

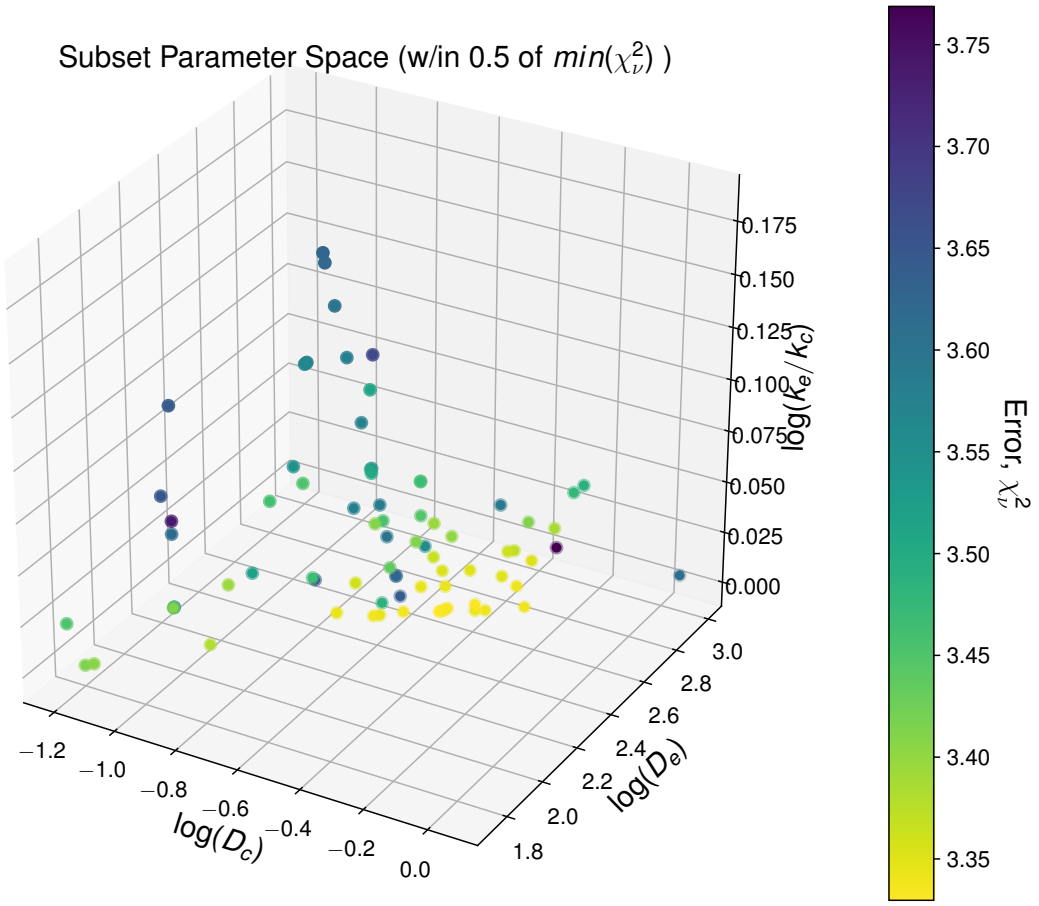

Figure S23. Candidate solution parameter space for the case with fracture density 0.020%.

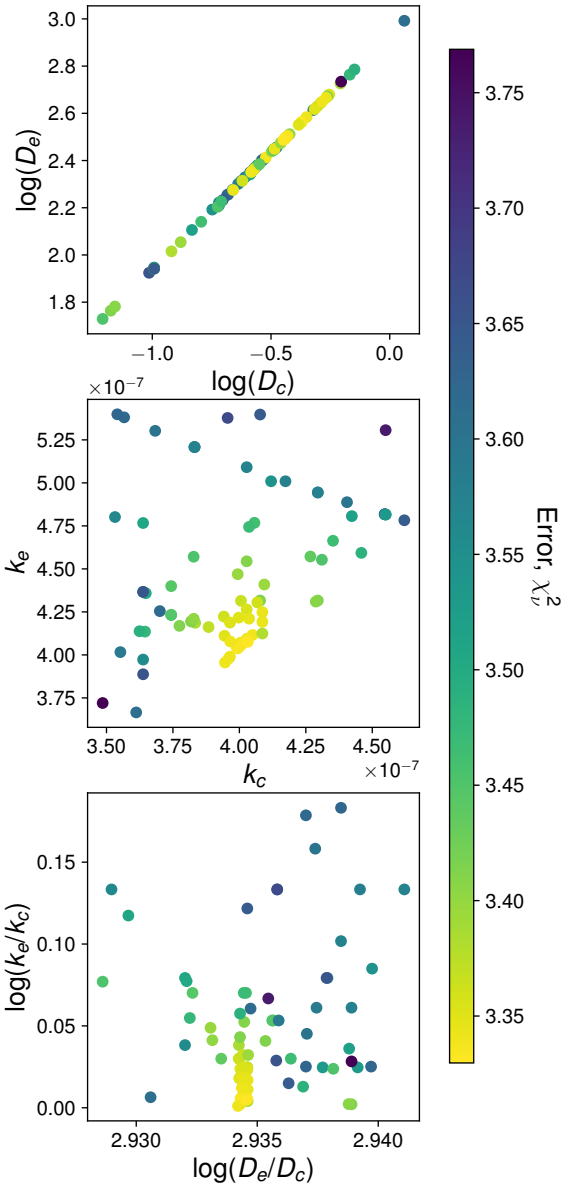

Figure S24. Comparison of individual atmospheric mixing parameters within the candidate solution parameter space for fracture density 0.020%.

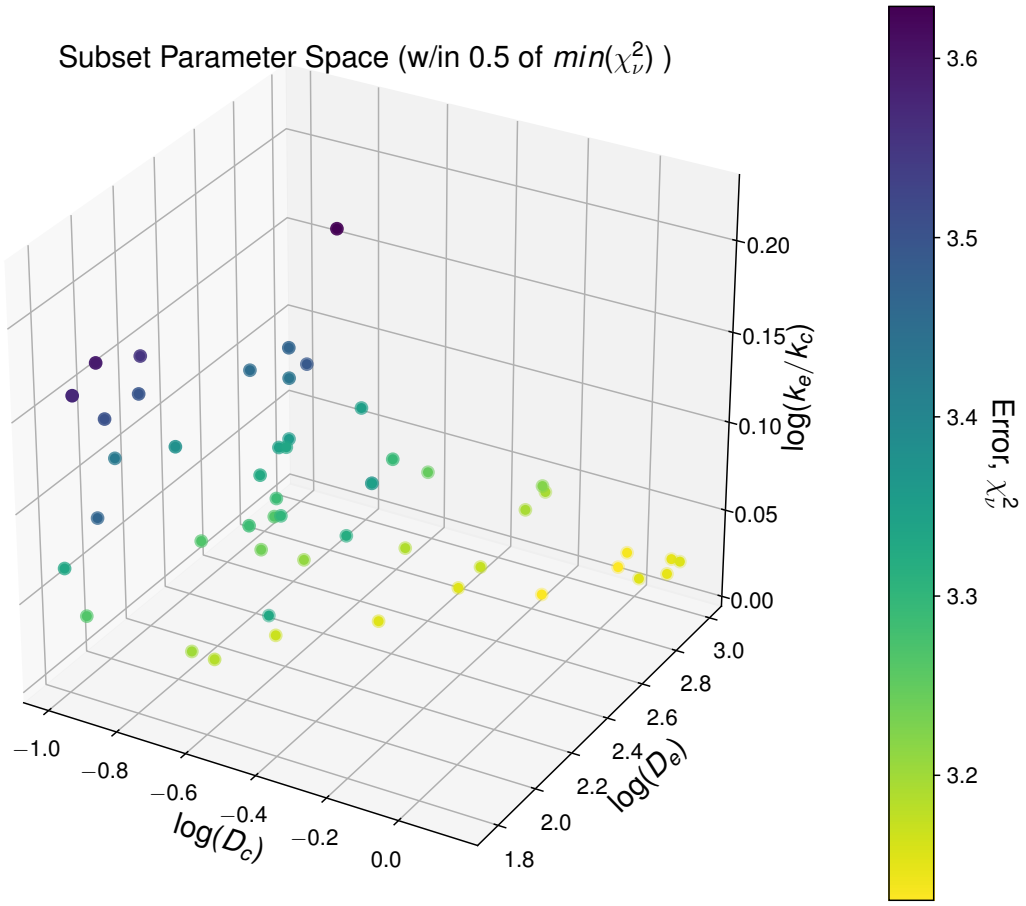

Figure S25. Candidate solution parameter space for the case with fracture density 0.035%.

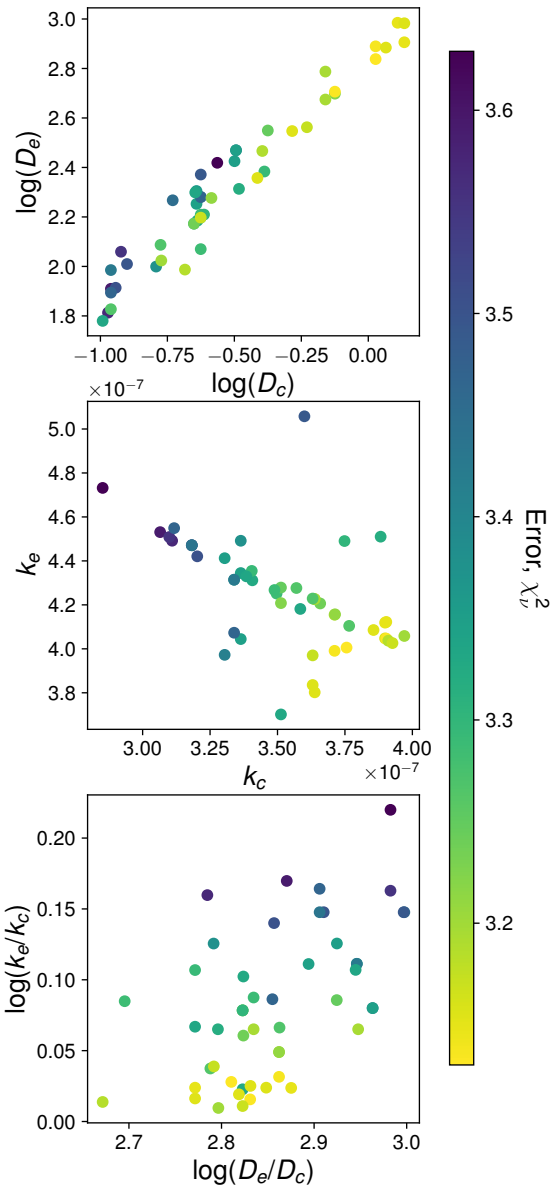

Figure S26. Comparison of individual atmospheric mixing parameters within the candidate solution parameter space for fracture density 0.035%.